

THE RADIAL VELOCITY CURVE AND PECULIAR TiO DISTRIBUTION OF THE RED SECONDARY STAR IN Z CHAMAELEONTIS

RICHARD A. WADE¹

Steward Observatory

AND

KEITH HORNE¹

Space Telescope Science Institute

Received 1987 May 22; accepted 1987 June 26

ABSTRACT

The secondary star of the dwarf nova Z Cha has been detected with the CCD spectrograph of the CTIO 4 m telescope. The TiO $\lambda 7150/\lambda 7650$ band ratio implies a Boeshaar spectral type of M5.5 for the secondary star, which contributes $\sim 15\%$ of the light at $\lambda 7500$. The absolute absorption strength of TiO is very weak on the side of the star that faces the white dwarf and accretion disk. The standard treatment of reflection effects, in which a fraction of the incident flux is thermalized and reradiated locally, predicts the opposite effect. Cross-correlation of the Na I $\lambda 8183, 8194$ doublet gives a heliocentric radial velocity curve with $\gamma = -23 \pm 15 \text{ km s}^{-1}$; $K = 443 \pm 15 \text{ km s}^{-1}$, to which must be added a correction of $-13 \pm 4 \text{ km s}^{-1}$ to account for the uneven line strength on the stellar surface. The corrected value of $K_2 = 430 \pm 16 \text{ km s}^{-1}$, combined with the mass ratio and inclination determined in the eclipse analysis published by Wood *et al.* in 1986, yields masses $M_1 = 0.84 \pm 0.09$ and $M_2 = 0.125 \pm 0.014 M_\odot$ for the white dwarf and secondary star, respectively. The secondary star lies close to the computed evolutionary tracks in the period-mass diagram published by Paczyński and Sienkiewicz in 1981.

The redundant observational constraints do not yield a consistent model for Z Cha unless standard assumptions are relaxed. The 3σ discrepancy between our spectroscopic masses and the lower masses derived from eclipse data by Wood *et al.* may imply that the primary star seen in the eclipse data is $50\% \pm 15\%$ larger than a Hamada-Salpeter white dwarf. The observed splitting of double-peaked emission lines corresponds to a velocity that is $70\% \pm 10\%$ of the Keplerian velocity at the outer edge of the accretion disk. The radial velocity curve of the emission lines has a larger amplitude and a phase shift relative to the true orbit of the white dwarf.

As a byproduct of this investigation, we present data on M dwarf spectra in the wavelength region $\lambda 7150\text{--}8800$.

Subject headings: stars: binaries — stars: dwarf novae — stars: individual (Z Cha)

1. INTRODUCTION

Z Chamaeleontis (1950: $8^{\text{h}}08^{\text{m}}50^{\text{s}}.1$, $-76^\circ 23' 09''$; the western star of a close pair, $\rho = 5''$) is an eclipsing, short-period binary system ($P = 107$ minutes) containing a white dwarf and a cool, low-mass secondary star. As a member of the SU UMa subclass of dwarf novae, it shows outbursts and superoutbursts (and superhumps during superoutbursts). Its particular importance lies in the fact that its eclipses distinctly show the separate ingress and egress of the white dwarf and of the bright spot at the edge of the accretion disk surrounding the white dwarf (Warner 1974). Thus for Z Cha the masses and other system parameters can be determined from precise photometric measurements and independently from spectroscopy, giving consistency checks on various assumptions that must be made to derive the masses of other interacting binary stars, for which such redundant information is generally not available.

Milestones in the study of Z Cha include the use of its quiescent and outburst eclipse light curves to develop the "standard model" of accretion disks in cataclysmic variable

systems (Bath *et al.* 1974); the exploitation of the compact nature of the white dwarf to make very precise eclipse timings (Bailey 1979; Cook and Warner 1981); the detection of the secondary star through its ellipsoidal variations (Bailey *et al.* 1981); the use of time-resolved spectroscopy of the emission lines to demonstrate that the accretion disk rotates in a quasi-Keplerian sense (Rayne and Whelan 1981); the suggestion that superhumps are the result of an eccentric ring formed during superoutbursts (Vogt 1982); a reconstruction of the *UBV* surface brightness distribution of the disk during outburst by an "eclipse mapping" technique (Horne and Cook 1985); and the analyses of the double-eclipse structure in the light curve to estimate the mass ratio and other properties of the system (Ritter 1980; Cook and Warner 1984; Wood *et al.* 1986). (For reviews of cataclysmic variables in general, see, e.g., Robinson 1976; Córdova and Mason 1983; Patterson 1984; and Wade 1985.)

Using fast photometry of the eclipses of Z Cha, Wood *et al.* (1986) derived the mass ratio and orbital inclination of the system ($6.54 < M_1/M_2 < 6.85$, $81.9^\circ > i > 81.6^\circ$; M_1 is the mass of the white dwarf), used a self-consistent estimated distance to the system $d = 97 \pm 15 \text{ pc}$ (Bailey *et al.* 1981; Horne and Cook 1985) to measure the temperature, radius, and mass of the white dwarf primary star ($M_1 = 0.54 \pm 0.01 M_\odot$), and

¹ Visiting Astronomer, Cerro Tololo Inter-American Observatory, National Optical Astronomy Observatories, operated by Associated Universities for Research in Astronomy, Inc., under contract with the National Science Foundation.

inter alia predicted that the heretofore unmeasured radial velocity semi-amplitude of the secondary star (hereinafter referred to as Z Cha B) should be $K_2 = 371 \pm 3 \text{ km s}^{-1}$. Their analysis also predicts that the semi-amplitude of the white dwarf should be $K_1 = 55 \pm 2 \text{ km s}^{-1}$; the most recent measurement of K_1 (actually of K_{em} , from the emission lines arising from the disk around the white dwarf) is $\sim 90 \text{ km s}^{-1}$ (Marsh, Horne, and Shipman 1987). However, the use of emission-line velocities in dynamical studies of cataclysmic variables has been suspect for some years (see, e.g., Wade 1985), because the velocity curves lag behind the expected orbital motion of the white dwarf (Stover 1981; Watts *et al.* 1986, and references therein) and the velocity amplitude is dependent upon which parts of the emission-line profile are measured (Shafer 1983; see also Watts *et al.* 1986). A direct measurement of K_2 is better suited to the task of establishing whether the eclipse analysis is correct.

Bailey *et al.*'s (1981) discovery of the ellipsoidal variations at infrared wavelengths showed that the secondary star is accessible to observation, at sufficiently long wavelengths. Bailey *et al.* deduced an approximate effective temperature of 2400 K and estimated that the star contributes $\sim 30\%$ of the light at $\lambda 8200$. An earlier study of the dwarf nova U Gem (Wade 1981), where light from the dM5 secondary star dominates longward of $\lambda 7300$, showed that the near-infrared Na I doublet ($\lambda\lambda 8183, 8194$) can be used to measure the velocity of M-type secondary stars in cataclysmic variables; and recent improvements in detector sensitivity (CCDs!) encouraged us to attempt a similar study of Z Cha.

An observing run in 1984 March, using the CTIO 4 m Ritchey-Chrétien spectrograph with the Singer camera, established the feasibility of measuring K_2 in Z Cha: by shifting (in wavelength) and summing together many short integrations of the near-infrared spectrum we were able to see the characteristic spectrum of a dM star, considerably diluted by light from the white dwarf and accretion disk (Horne 1986). These data were nevertheless rather noisy, and because of unfavorable weather we obtained too few observations to justify a more thorough analysis. A second observing run at CTIO in 1985 March used the Air Schmidt camera in place of the Singer camera; the significantly higher throughput (and better weather) gave us a much better data set, which we analyze in detail in this paper.

The plan of the paper is as follows. In § II we describe the observations and data reduction techniques, giving special attention to points of technique which are perhaps slightly unusual and which we feel were important to the success of the experiment. In § III we compare spectra of the secondary star in Z Cha with those of isolated M dwarfs, use cross-correlation techniques to measure the velocity of the secondary star as a function of orbital phase, and examine the photometric variations of spectral features with orbital phase. In § IV we model

the phase variations of the absorption features in terms of their surface distribution on the secondary star, evaluate a correction to the observed K velocity to account for the nonuniform line strength, derive physical parameters of the Z Cha binary, and discuss discrepancies with previous measurements. We summarize the main results of the paper in § V.

II. OBSERVATIONS

Z Cha was in its quiescent state during our observations on UT 1985 March 1 and 2, 2 weeks after the outburst that began on February 13 and 1 week before the outburst that began on March 9 (Bortle 1985*a, b*). Table 1 summarizes the observations. We obtained a total of 47 spectra of Z Cha, covering $\lambda\lambda 7160\text{--}8800$ with 6 \AA resolution. The 300 s integration time was long enough to reduce the impact of the readout noise (20 electrons rms) and the dead time (60 s) required for readout and preparation of the CCD between exposures, yet short enough to prevent significant velocity smearing from the orbital motion of Z Cha. We attempted to limit systematic errors so that the short exposures could be summed to build up a high S/N spectrum.

Spectra of a comparison star were obtained simultaneously with the Z Cha spectra, at positions $61''$ apart on the $1''.5$ wide spectrograph slit. This procedure served to check the stability of our radial velocity measurements, and permitted accurate relative spectrophotometry despite the presence of patchy thin clouds on March 2 and the use of a slit narrower than the $2''.1$ FWHM seeing disk.

We also obtained spectra of K and M type stars for use in estimating the spectral type of the secondary star in Z Cha, for use as cross-correlation templates for velocity determinations, and to establish the instrumental velocity zero-point. Relevant information from the literature on these stars is collected in Table 2.

Our instrumental setup, observing, and data reduction techniques are described in greater detail below. Items of special interest are the optimal spectrum extraction procedure, described in § IIc, techniques for the removal of telluric absorption lines, § IIe, and methods for obtaining spectrophotometry through a narrow slit by trailing standard flux stars across the slit, § II*f*, and by rotating the position angle of the slit to observe simultaneously a comparison star, § II*g*.

a) Instrumentation

The observations were made using the GEC charge-coupled device (CCD) known as EPI 3. This unthinned CCD has a detecting surface that is divided into a 385 column by 576 row array of pixels, each $22 \mu\text{m}$ square. CCDs have high quantum efficiency in the spectral region of interest. They have no count-rate limitations, and each pixel can accumulate a large number of electrons in its "well" before saturation effects are important, so that relatively bright stars can be observed for cali-

TABLE 1
CCD SPECTROPHOTOMETRY OF Z CHAMAELEONTIS

Date	Begin UT	End UT	Hour Angle End (West)	Number of Exposures	Begin Phase	Phase Interval
UT 1985 Mar 1	04:06	06:09	03:53	18	0.78	1.15
	07:12	08:10	05:55	9	0.51	0.54
UT 1985 Mar 2	02:29	04:43	02:31	20	0.30	1.25

NOTE.—All exposures were 300 s, with the spectrograph slit at position angle $163^\circ 6$.

TABLE 2
STARS USED AS SPECTRAL TYPE OR VELOCITY STANDARDS

Star	V^a	$V-R^b$	$R-I^b$	Sp ^c	$v_r(\text{Gliese})^d$ (km s ⁻¹)	$v_r(\text{SH})$ (km s ⁻¹)	Alias
Gliese 406	13.46	2.29	1.76	M6e	+13 C	...	Wolf 359
Gliese 551	11.05	...	1.65	M5.5e	-16 C	...	Proxima Cen
Gliese 234AB	11.08	1.59	1.38	M4.5e	+24 C	15.4	Ross 614
Gliese 447	11.14	1.56	1.35	M4+	-13 C	-31.9	Ross 128
Gliese 285	11.18	1.52	1.35	M4.5e	+18 B	26.4	YZ CMi
Gliese 299	12.77	...	1.30	M4-4.5	-35 C	...	Ross 619
Gliese 273	9.87	1.37	1.22	M4	+26 C	19.0	BD +5°1668
Gliese 381	10.80	M3	L968-22
Gliese 250B	10.07	1.13	0.99	M2.5	-10 B	...	HD 50281
Gliese 393	9.64	1.12	0.97	M2	+12 B	6.5	BD +1°2447
Gliese 382	9.25	1.10	0.92	M2	+12 B	6.7	BD -3°2870
Gliese 229	12.8	...	0.82	M1	+4 B	...	HD 42581
Gliese 328	9.96	0.90	0.67	M0.5	+3 C	-4.1	BD +2°2098
HD 67790	8.1	K2	+51.0
HD 105699	7.0	K2	-20.6

^a V magnitude from Stauffer and Hartmann 1986 if available, otherwise Gliese 1969 or Griffin 1971; K stars.

^b $V-R$ and $R-I$ from Stauffer and Hartmann 1986, or $R-I$ alone from Gliese 1969. Ordering is by $R-I$ color; Gliese 381 is placed in sequence based on the Boeshaar 1976 spectral type. R and I are on the Kron system.

^c Spectral type from Boeshaar 1976, except HD types for 67790 and 105699.

^d Radial velocity quoted in Gliese 1969, except HD 67790 and 105699 where velocity is from Griffin 1971; letter is a quality index.

^e Radial velocity from Stauffer and Hartmann 1986.

bration. Because readout occurs only at the end of an exposure, there is no need to restrict the active area of the detector due to bandwidth limitations, and the two-dimensional format can be used efficiently to achieve a very accurate estimate of the sky brightness (long-slit mode). These properties taken together mean that, for brighter stars and even faint stars observed in a single long exposure, well-calibrated data of high signal-to-noise (S/N) ratio can be obtained. Interference fringes are not a source of concern with the GEC CCD we used. On the other hand, CCDs suffer from amplifier readout noise and deferred charge transfer, and precautions were taken to minimize the damage these effects might do to short observations of faint targets.

We used grating 181 (316 grooves mm⁻¹) in the Ritchey-Chrétien spectrograph of the CTIO 4 m telescope to observe the spectral region $\lambda\lambda 7160-8800$. A Schott RG610 filter was used below the slit to isolate the first spectral order and to reduce stray light in the spectrograph. Another RG610 filter was used in front of the TV slit-viewing system to reduce the possibility of guiding errors resulting from atmospheric dispersion. With the Air Schmidt camera and grating 181, each 22 μ m pixel of the CCD sampled 0".74 along the slit and 2.9 \AA in the dispersion direction. To reduce the effect of readout noise, we used on-chip binning of 2:1 in the spatial direction, giving "super-pixels" of effective size 1".5 by 2.9 \AA , more nearly matched to the seeing disk. The 225 μ m slit width corresponded to 1".47 at the focal plane of the telescope, and with the grating magnification taken into account projected to 39 μ m (1.8 pixels) on the CCD, giving a spectral resolution of 5-6 \AA . This resolution compared well with the 6 \AA FWHM measured from comparison lines. The focus was slightly better at the blue end of the spectrum.

Each readout of the CCD produced an image containing 140 columns (spatially distinct) by 576 rows (dispersion direction) of astronomical data and some additional "waste" columns or overscan rows. The overscan rows were used to

measure a bias level which was subtracted from each pixel of the image before further processing.

In addition to the binning of columns described above, we briefly exposed the CCD to light from an LED (inside the Dewar) at the beginning of each exposure. This "preflashing" effectively doubled the background noise, but improved the charge transfer properties of the device at low exposure levels.

b) Picture Processing

Zero-length preflashed exposures, or "bias frames," measure both the intrinsic fixed pattern of the CCD and the pattern of charge deposited by the LED. About 50 bias frames were obtained on each night. The bias level was determined from the overscan regions of the frame and subtracted from each pixel; the overscan regions were then trimmed from the frame. The "bias frames" were combined by median and mean filtering to form a nearly noise-free image of the remaining fixed pattern, which was subtracted from the remaining frames.

About 20 "flat-field" frames were obtained each night by observing an illuminated white spot on the inside of the 4 m dome. The frames were filtered to produce a master flat-field image. A smooth curve was fitted to represent approximately the average wavelength variation of the flat-field data, and each column of the master flat-field image was divided by this polynomial. The inverse of this normalized image is the "balance-factor" frame; it represents the moderate-scale and pixel-to-pixel variations in sensitivity of the device. All stellar data and wavelength calibration frames were multiplied by these balance factors to remove these variations, but since the balance factors typically differed from unity by only a few percent, the count-rate information in the image (which is usually a strong function of wavelength, and sometimes a function of position along the slit) was retained for subsequent use in error analysis.

Each stellar data frame was then treated to remove the sky contribution. Columns containing sky signal alone were desig-

nated, and interpolating polynomials were fitted row by row to make estimates of the sky signal in columns containing the stellar spectrum. For our data, we found a second-order interpolating polynomial to be adequate. This procedure makes full use of the long-slit capability of the CCD to produce a nearly noise-free estimate of the sky level, pixel by pixel.

c) Spectrum Extraction

Our procedure for extracting one-dimensional spectra from the CCD images closely follows the methods for optimal extraction described by Horne (1986), to which the reader is referred for details. The seeing conditions gave rise to spectra spread over five adjacent columns, but with most of the signal concentrated in one or two columns. Each column was treated as an independent measurement of the spectrum, but multiplied by a wavelength-dependent factor representing the fraction of the signal that is received in that column. The slow wavelength dependence of the column weights reflects changes in the seeing profile due to optical distortions, variations in focus, and atmospheric dispersion displacing the successive monochromatic images along the slit. A smooth, stable, and accurate model of the seeing profile was generated for each exposure by fitting polynomials to an initial estimate of the normalized weights along each column. An iterative, variance-weighted fitting scheme was used to reject portions of the image that were flawed, e.g., "blocked" columns and cosmic ray hits. The polynomials were then used to correct for the fraction of the starlight falling on each column, and to determine optimal weights for combining the five columns at each wavelength. Thus the relatively noisy columns in the wings of the stellar profile were given less weight than the columns containing most of the flux, yet the one-dimensional extracted fluxes are accurate because a weighting scheme normalized to unity was used.

The variance estimates included a uniform contribution from readout and preflash noise and photon statistics from the object and (underlying) sky. The readout noise (7 digital units) and gain (3.5 electrons per digital unit) were determined by examining the pixel-to-pixel fluctuations in bias and flat-field frames after treatment with the master bias and balance-factor frames. In addition to allowing proper weighted extraction of spectra, careful estimation of the point-by-point variance of the data makes subsequent statistical error analysis possible.

Horne (1986) shows a well-exposed spectrum of a bright standard star and a typical 300 s exposure of Z Cha, extracted both by the optimal procedure and by the usual extraction method using a fixed number of columns. The optimal extraction procedure removed most blemishes and gave significantly improved signal-to-noise ratios for weak exposures. We found it necessary to mask a few cosmic-ray blemishes that were not completely rejected by the optimal extraction algorithm. These were located by comparing each spectrum with a median-smoothed version of itself and rejecting pixels lying many standard deviations from the smoothed curve. Four of the 47 spectra were "corrected" in this way.

d) Wavelength Calibration

Wavelength calibration of each stellar spectrum was done using fits to the positions of lines in helium-argon spectra, which were observed throughout the night and at the beginning and end of each night. One-dimensional arc spectra were extracted from the same CCD columns with the same extraction weights as the stellar spectra for which they were used, to

guard against geometric or optical distortions. A fourth-order polynomial fitted 14 He-Ar comparison lines with a typical rms residual of 0.05 Å. A master wavelength polynomial for each night was derived from the average of all the arc spectra, and small corrections were made to the three lowest-order polynomial coefficients to fit the individual arc spectra and to interpolate the calibration in time to the epoch of each stellar spectrum.

The stability of the calibration against flexure was excellent, the lines shifting smoothly and by small amounts (a few times 0.1 Å) over periods of hours during continuous tracking of a target. After moving from one target to another, however, or rotating the position angle of the spectrograph slit, we found shifts of up to 1 pixel. We were careful always to make comparison lamp observations at each position of the telescope and before and after any spectrograph rotations.

e) Atmospheric Corrections

Our radial velocity measurements of the weak Na I $\lambda\lambda 8183, 8194$ doublet, which is obscured by a forest of telluric water vapor lines, would have been impossible without the empirical correction scheme described below. To each spectrum we applied a correction to account for the continuous atmospheric absorption, scaled to the appropriate airmass. This correction for continuous atmospheric absorption leaves a multitude of sharper telluric features in the stellar spectra, including the A and Z bands and anonymous water vapor bands in the region $\lambda\lambda 7150-7400$ (see Curcio, Drummeter, and Knestrick 1964 for a high-resolution atlas of absorption in the lower atmosphere; additional species, such as O I, exist at higher altitudes, and their lines are not included in the atlas).

To aid in removing the telluric line features we made observations of the OB stars HD 64722, HD 135591, and HD 86606 at several different airmasses. These stars have relatively few intrinsic spectral features in regions of interest to us, and thus serve as smooth continuum lamps above the atmosphere. The metal-deficient flux standard stars are useful in this regard as well. We first identified wavelength bands that were free of atmospheric absorption (i.e., showed nothing in a ratio spectrum of a star observed at both low and high airmass). We fitted an interpolating spline through the upper envelope of these "continuum" regions and in the remaining spectral regions derived for each observation the logarithmic quotient spectrum of the telluric absorption, which shows the absorption in magnitudes as a function of wavelength.

The effect of the telluric lines on the observed spectrum can be modeled as

$$(\text{observed flux}) = (\text{incident flux}) \exp [-\tau(\lambda)(\sec z)^{\alpha}].$$

Optically thin absorption corresponds to $\alpha = 1$, and the highly saturated telluric lines are expected to have equivalent widths that grow approximately in proportion to the square root of the airmass ($\alpha = \frac{1}{2}$). From observations at airmasses between 1.0 and 2.0 we found the average value of α to be near 0.6 for the A band (close to saturation), and used $\alpha = 0.6$ to describe the water vapor absorption too. Figure 1 shows the adopted $\tau(\lambda)$ relation for March 1, along with the residual absorption in the corrected spectra of the OB and flux standard stars (using $\alpha = 0.6$). This empirical correction scheme worked remarkably well, except in the very strong core of the A band. Much of the other residual absorption is presumably due to the time-variable optical path length of water vapor.

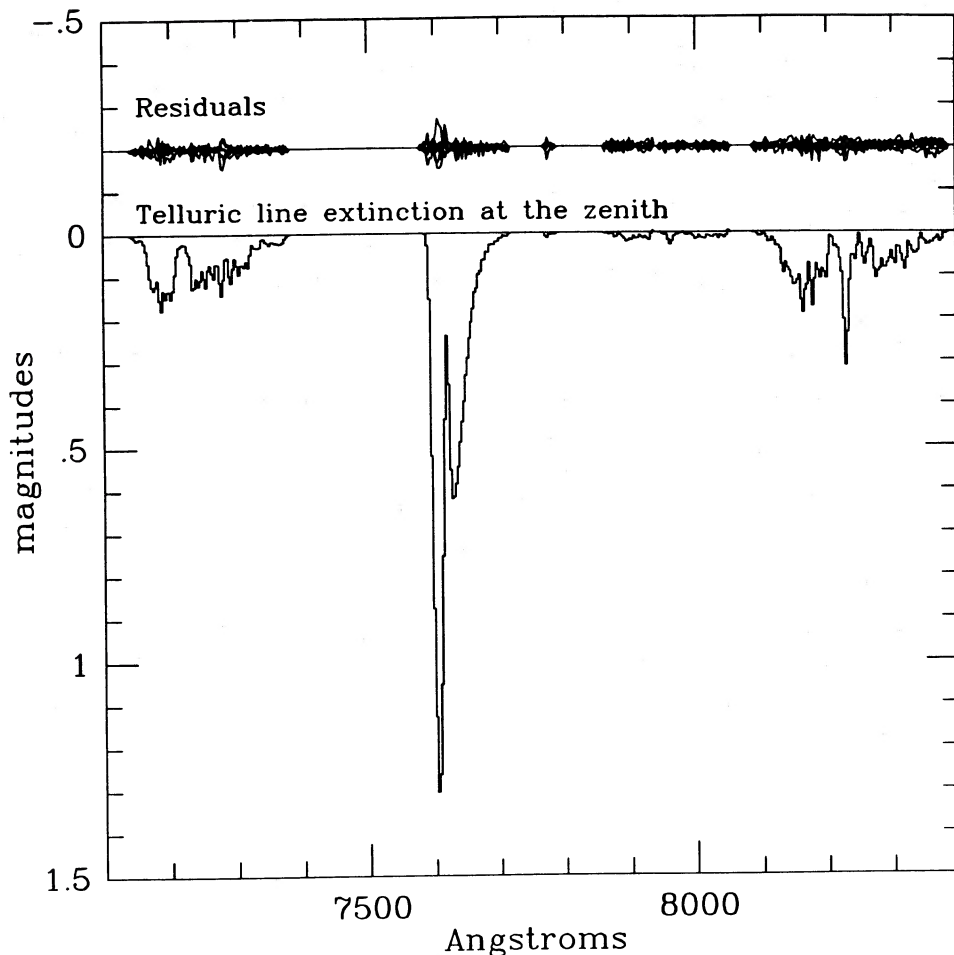


FIG. 1.—The fine structure in the telluric absorption spectrum, according to the model adopted for 1985 March 1. (*lower part of figure*) Magnitudes of extinction at airmass 1.0, as a function of wavelength. The absorption is assumed to grow with increasing airmass as $(\sec z)^{0.6}$. (*upper part of figure*) Residual absorption in the spectra of seven standard stars observed on March 1.

f) Flux Calibration

A precaution we took for this radial velocity study was not to change the slit width. (Experience shows that the width is not accurately reproducible at the KPNO 4 m RC spectrograph.) This required that we adopt an unusual procedure for observing spectrophotometric standard stars. Normally one observes such stars through a wide slit to ensure that the entire seeing image is sampled and to counteract the effects of atmospheric dispersion. We achieved the same result by trailing the star image *across* a slit of known width at a known angular rate. Better results were obtained by making multiple passes at a high rate, to average out fluctuations in the seeing disk. In this last manner, we observed at least one of the flux standards HD 84937 and HD 140283 (Oke and Gunn 1983) each night, as well as the comparison star of Z Cha.

The digital counts in each spectral pixel were corrected for continuous atmospheric extinction and converted to instrumental magnitudes using an arbitrary zero-point. Observations of the Oke-Gunn flux standard stars were then used to place all the observations on the AB79 spectrophotometric system (Oke and Gunn 1983). (Of course, the narrow slit and the presence of thin clouds on the night of March 2 means that these data are calibrated for correct relative fluxes only, not absolute fluxes.) The AB79 magnitude required to produce one

count $\text{s}^{-1} \text{\AA}^{-1}$ decreased smoothly from 16.7 at $\lambda 7100$ to 14.9 at $\lambda 8800$ and was constant from night to night to within measurement uncertainties of $\pm 5\%$.

g) Slit Corrections

By a suitable rotation of the slit position angle, we were able to obtain spectra of a comparison star simultaneously with the spectra of Z Cha. This permitted us to monitor the slit throughput, which varied as a function of time due to guiding errors, changing seeing, and changing transparency. The star used for this purpose, dubbed "Z Cha Amiga," has a similar brightness to Z Cha and is located $\sim 61''$ away in P.A. 344° . Its spectral type is G or K; the luminosity class is unknown. The Amiga spectra also served as a check for velocity errors.

The count rate observed on the Amiga fluctuated by $\sim 20\%$ from one 300 s exposure to the next and varied by $\sim 50\%$ over time scales of an hour. These variations demonstrate the dangers of *unmonitored* "Cassegrain slit-photometry" (see, e.g., Schneider and Young 1980) and attest to the importance of using a comparison star to ensure accurate spectrophotometry.

We obtained a photometric spectrum of the Amiga by driving the slit repeatedly across its position, in the same way that we measured the spectrophotometric standard stars. We assume that the slit throughput correction is a smooth function

of wavelength but varies rapidly with time. The slit throughput spectrum for each observation is then given by the ratio of the slit spectrum of the Amiga to the photometric spectrum. Noise in the calibration was reduced by fitting a linear function in wavelength to this ratio spectrum.

The accuracy of the slit corrections depends on the precise placement of the slit position angle, for otherwise the variable and comparison star spectra sample different parts of the seeing profile. We expect that the final photometric accuracy is better than 5%, but tests with a pair of constant stars to establish the accuracy of the technique would be desirable.

III. RESULTS

a) The Spectrum of *Z Chamaeleontis B*

Figure 2 presents two orbit-averaged spectra of *Z Cha*, a spectrum of *Z Cha* during the white dwarf eclipse, and a spectrum of the dM5.5 star Proxima Cen. The two orbit-averaged spectra are "phased" spectra in the rest frames of the white dwarf and the companion star, permitting us to see the double-peaked emission lines from the accretion disk and the absorption spectrum of *Z Cha B* without the velocity smearing that would otherwise be induced by averaging around the orbit. The phased spectra were formed by first rebinning 44 individ-

ual 300 s spectra onto wavelength scales shifted to compensate for the assumed orbital motion, and then computing their average. We used the quadratic ephemeris of Wood *et al.* (1986) to compute binary phases, and adopted $K_1 = 60$ and $K_2 = 400$ km s $^{-1}$ to define the orbital frames of the white dwarf and *Z Cha B*, respectively (but see § IIIb). We gave equal weight to each of 20 intervals of orbital phase, rather than weighting each of the spectra equally. The three spectra that were averaged to form the spectrum in eclipse were omitted from the orbit averages.

The orbit-averaged spectrum in the white dwarf frame ($K_1 = 60$ km s $^{-1}$; displaced upward in Fig. 2 for clarity) shows prominent double-peaked emission in the Ca II triplet lines at $\lambda\lambda 8498, 8542$, and 8662 . The peak-to-peak separation of ~ 1200 km s $^{-1}$ causes the redshifted peak of $\lambda 8498$ to coincide with the blueshifted peak of $\lambda 8542$. The velocity splitting of the peaks is very similar to that seen in the Balmer emission lines (Rayne and Whelan 1981; Marsh, Horne, and Shipman 1987), and probably represents twice the orbital velocity at the outer rim of the accretion disk. A somewhat weaker display of double-peaked emission lines in the Paschen series makes the continuum difficult to define in this region. The P12 profile is clearly visible, but P13, 15, and 16 nearly coincide with the three Ca II lines, and P14 falls in the notch between $\lambda 8542$ and

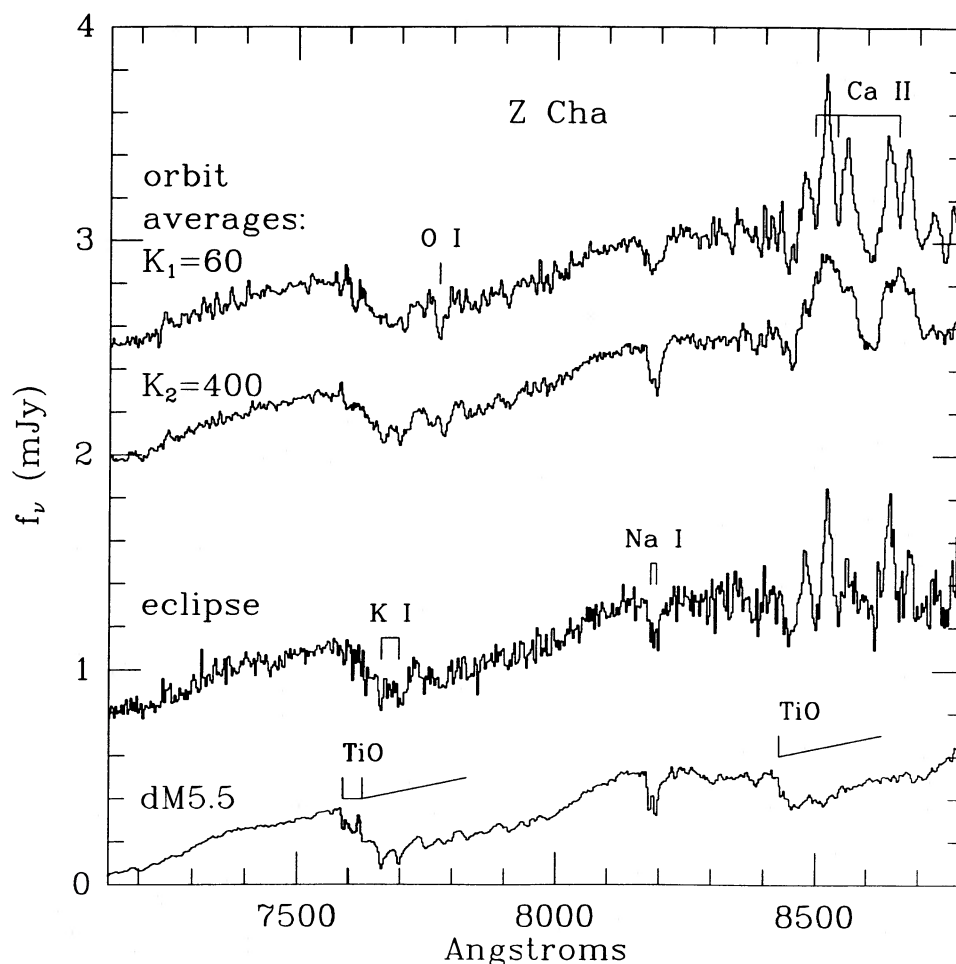


FIG. 2.—(top to bottom) Orbit-averaged spectra of *Z Cha* (uniformly weighted over $0.025 < \phi < 0.925$) in the rest frame of the white dwarf ($K_1 = 60$ km s $^{-1}$; shifted up by 0.5 mJy) and in the rest frame of the secondary star *Z Cha B* ($K_2 = 400$ km s $^{-1}$); also, the average of three spectra of *Z Cha* taken during eclipse, and the spectrum of a dM5.5 star (scaled to 0.3 mJy at $\lambda 7500$). The accretion disk produces double-peaked Ca II $\lambda\lambda 8498, 8542, 8662$ and Paschen emission lines. *Z Cha B* produces TiO bands and Na I $\lambda\lambda 8183, 8194$ and K I $\lambda\lambda 7664, 7698$ lines similar to those in the dM5.5 spectrum. Weak O I $\lambda 7774$ absorption also is present.

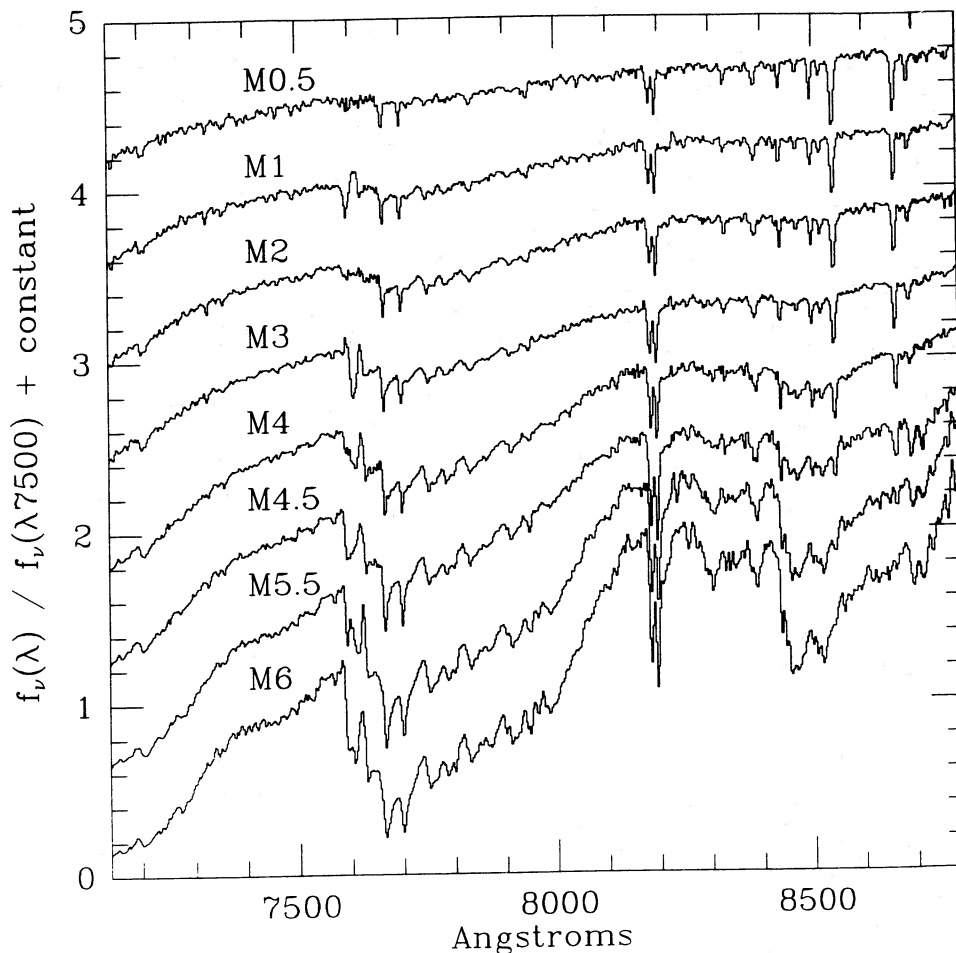


FIG. 3.—A sequence of M dwarf spectra normalized to unity at $\lambda 7500$ and offset vertically by multiples of 0.5

$\lambda 8662$. The pseudo-continuum formed by the blended emission of higher members of the Paschen series appears to connect continuously with the Paschen continuum at $\lambda 8206$. The emission lines visible in the eclipse spectrum arise from the unocculted outer parts of the accretion disk. Subtracting the eclipse spectrum from the orbit-averaged spectrum leaves a spectrum (not shown) that is approximately flat between $\lambda 7150$ and $\lambda 8800$, when plotted as f_v .

Absorption features of an M star are apparent in both the orbit-averaged spectra and the spectrum during eclipse. Most noticeable are the TiO band structure at $\lambda\lambda 7150, 7600, 8450$, and the Na I doublet at $\lambda\lambda 8183, 8194$. The profile of the Na I doublet line is sharpest in the orbit-averaged spectrum for the rest frame of Z Cha B ($K_2 = 400 \text{ km s}^{-1}$). A comparison with the series of M star spectra shown in Figure 3 indicates that Z Cha B is of fairly late spectral type.

We made a quantitative estimate of the spectral type of Z Cha B by measuring absorption features in the Z Cha spectra and in the spectra of the dM stars that we observed. Young and Schneider (1981) show that the TiO $\lambda 7150/\lambda 7600$ ratio is a good indicator of spectral type in M dwarfs. Equivalent widths of the absorption features cannot be used directly, because they are affected by the strong continuum from the white dwarf and accretion disk, but *flux deficits* relative to a reference continuum are not affected. Our desire to cover the Ca II region

prevented measurements of the continuum near $\lambda 7000$. We therefore defined the reference continuum $c_v(\lambda)$ by fitting a least-squares straight line to the data $f_v(\lambda)$ in the continuum bands ($\lambda\lambda 7450\text{--}7550$), ($\lambda\lambda 8130\text{--}8170$) and ($\lambda\lambda 8222\text{--}8262$), the later pair of which straddles the Na I doublet. Flux deficits between this reference continuum and the observed spectra were then obtained by averaging between definite wavelength limits in the rest frame of each star. The three quantities of interest are flux density deficits in the TiO bands

$$d_v(\lambda 7165) = \frac{\int_{7140}^{7190} [c_v(\lambda) - f_v(\lambda)] d\lambda/\lambda}{\int_{7140}^{7190} d\lambda/\lambda}$$

and

$$d_v(\lambda 7665) = \frac{\int_{7640}^{7690} [c_v(\lambda) - f_v(\lambda)] d\lambda/\lambda}{\int_{7640}^{7690} d\lambda/\lambda},$$

and the integrated flux deficit of the Na I doublet

$$j(\text{Na I}) = \int_{8170}^{8220} [c_v(\lambda) - f_v(\lambda)] \frac{cd\lambda}{\lambda^2}.$$

Our measurements of M dwarfs are assembled in Table 3. For each observation the Gliese number and Boeshaar spectral type are identified in columns (1) and (2). Columns (3) and (4) give the TiO flux density deficits, normalized by the continuum

TABLE 3
M. DWARF MEASUREMENTS

STAR (Gliese) (1)	Sp (Boeshaar) (2)	TiO $\lambda\lambda 7165$		Ratio $d_v(\lambda 7665)/d_v(\lambda 7165)$ (5)	TiO $\lambda\lambda 7165$		Na I $\lambda\lambda 8170-8220$		TiO $\lambda\lambda 7580-8130$	
		$d_v(\lambda 7165)$	$d_v(\lambda 7665)$		$d_v(\lambda 7165)$	$d_v(\lambda 7665)$	j		j	
		$c_v(\lambda 7500)$ (3)	$c_v(\lambda 7500)$ (4)		$c_v(\lambda 7165)$ (6)	$c_v(\lambda 7665)$ (7)	$c_v(\lambda 7500)$ (10 ¹¹ Hz) (8)	EW (Å) (9)	$c_v(\lambda 7500)$ (10 ¹¹ Hz) (10)	EW (Å) (11)
406	M6e	0.367	0.812	2.21	0.685	0.657	8.21	9.4	162	231
551	M5.5e	0.434	0.676	1.55	0.685	0.571	6.47	8.3	124	189
	M5.5e	0.429	0.668	1.55	0.679	0.564	6.48	8.3	125	190
234AB	M4.5e	0.434	0.440	1.01	0.587	0.388	4.62	6.7	75.9	125
285	M4e	0.444	0.434	0.97	0.589	0.386	4.24	6.3	80.7	134
477	M4+	0.446	0.400	0.89	0.579	0.359	4.10	6.2	66.7	113
	M4+	0.456	0.398	0.87	0.586	0.359	3.87	6.0	65.5	112
299	M4-4.5	0.426	0.392	0.91	0.553	0.352	3.96	6.0	61.9	105
273	M4	0.432	0.321	0.74	0.547	0.291	2.88	4.5	59.3	101
381	M3	0.352	0.186	0.53	0.413	0.173	2.18	3.8	31.2	56
250B	M2.5	0.319	0.176	0.55	0.373	0.164	1.97	3.4	30.7	55
393	M2	0.354	0.149	0.42	0.408	0.140	1.70	3.0	24.6	45
382	M2	0.318	0.143	0.45	0.364	0.134	1.88	3.4	23.8	43
	M2	0.302	0.144	0.48	0.353	0.134	2.00	3.5	24.8	45
	M2	0.347	0.135	0.39	0.385	0.129	1.70	3.2	22.4	42
229	M1	0.234	0.114	0.49	0.267	0.108	1.88	3.4	20.4	37
	M1	0.244	0.101	0.41	0.278	0.095	1.84	3.3	17.5	32
328	M0.5	0.185	0.047	0.25	0.203	0.045	1.48	2.8	7.6	14
	M0.5	0.173	0.048	0.28	0.190	0.046	1.54	2.9	7.6	14

flux density at $\lambda 7500$ since we have only relative spectrophotometry of the M dwarfs. Column (5) is the TiO band ratio; columns (6) and (7) are fractional depths of the TiO bands relative to the local continuum; columns (8) and (9) are the integrated flux and equivalent width for the Na I doublet; and columns (10) and (11) for TiO $\lambda 7600$.

Figure 4 shows the TiO band strength $d_v(\lambda 7665)/c_v(\lambda 7665)$ plotted against the TiO band ratio $d_v(\lambda 7665)/d_v(\lambda 7165)$. The dM standard stars form a well-defined sequence, the fractional depth of the TiO band at $\lambda 7665$ and the $\lambda 7665/\lambda 7165$ TiO band ratio both increasing for later spectral types. These quantities for Z Cha in and out of eclipse are also plotted. Z Cha has the same TiO band ratio as a dM5.5 star, but the TiO bands are weaker because of dilution by the white dwarf, disk, and bright spot. As expected, the dilution is less during eclipse. Thus Z Cha B contributes $\sim 30\%$ of the light at $\lambda 7665$ during eclipse, but only $\sim 15\%$ averaged over the out-of-eclipse orbit.

The TiO band flux deficit ratio gives an unbiased estimate of the spectral type of Z Cha B even in the presence of the diluting continuum from the disk, unless the disk spectrum itself has TiO bands. The advantage of measuring flux rather than equivalent width was first exploited for cataclysmic variables by Young and Schneider (1979). Young and Schneider (1981) used a TiO band ratio very similar to ours but with a curved reference continuum rather than the linear one that we adopt. The TiO band ratio relative to our linear continuum is free of systematic effects, since the difference between the eclipse and orbit-average spectra of Figure 1 shows that the diluting light has a continuum f_v that is approximately linear in λ over our wavelength region, with no appreciable TiO bands.

b) The Velocity Curve of Z Chamaeleontis B

We measured the radial velocity curve of Z Cha B from the Na I absorption doublet at $\lambda\lambda 8183, 8194$. The Na I doublet carries most of the velocity information, as should be clear from Figure 2. The Ca II triplet lines at $\lambda\lambda 8498, 8542$, and 8662

are very weak at the M5.5 spectral type of Z Cha B, and in any case this part of the spectrum is confused by Ca II and Paschen emission lines from Z Cha's accretion disk. The TiO bands, K I $\lambda\lambda 7664, 7698$ and other features to the blue are more diluted and not as "sharp" as the Na I lines. The Na I doublet lies in the midst of a forest of water vapor lines, but these telluric lines have been adequately removed by the procedure described in § IIe. The Na I doublet was also used by Wade (1981) to measure the radial velocity curve of the dM5 secondary star in U Gem.

To measure radial velocities, we first rebinned each spectrum to remove the line-of-sight velocity of Earth relative to the Sun and to create a uniform velocity spacing of 100 km s^{-1} between adjacent pixels. Next we fitted and subtracted the continuum from each spectrum, and used one of the M dwarf spectra in the spectral region ($\lambda\lambda 8160-8220$) as a template against which we cross-correlated each of the 47 Z Cha and 19 M dwarf spectra. Finally, we defined velocities relative to the template by interpolating to find the peak of the cross-correlation function, and adopted an appropriate heliocentric velocity for the template (Table 2).

The orbital motion of Z Cha B can be seen in Figure 5, which presents cross-correlation functions obtained from spectra of Z Cha at 20 different binary phases. The auto-correlation function of the template spectrum, in this case Proxima Cen (dM5.5e), is shown at the bottom of the figure. The barely resolved Na I doublet structure produces ledges on each side of the autocorrelation peak and causes the cross-correlation functions to be broader than the expected instrumental resolution, which is about 3 pixels. (A much better resolved example of the triple-peaked autocorrelation function of the Na I doublet is shown in Fig. 1 of Wade 1985.)

It is not completely obvious how velocities should be measured from the cross-correlation functions. We measured velocities by two methods: (1) fitting a Gaussian template with $\sigma = 500 \text{ km s}^{-1}$, which roughly matches the width of the cor-

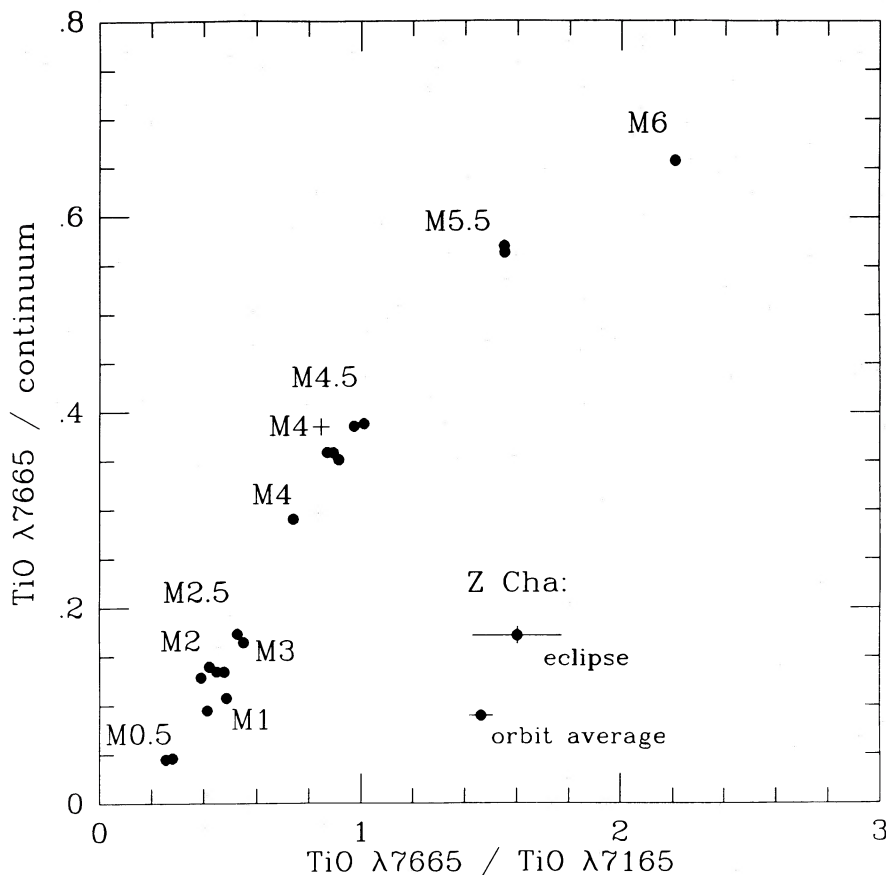


FIG. 4.—The fractional depth of the TiO $\lambda 7665$ band is plotted against the TiO band ratio for the M dwarf stars of Fig. 3 and for the orbit-averaged and eclipse spectra of Z Cha in Fig. 2. Multiple points generally represent repeated observations of the same star, except that two stars of spectral type M2 and M4+ were observed. The band ratio indicates a Boeshaar spectral type of M5.5 to M6 for Z Cha B, while the band depth implies that Z Cha B contributes only 30% of the light during eclipse and 15% out of eclipse.

relation function, and (2) fitting a narrow Gaussian with $\sigma = 100 \text{ km s}^{-1}$ to data points around the tip of the cross-correlation peak. The method 2 velocities have a smaller statistical uncertainty than the method 1 velocities. For the M dwarfs in our sample, the method 2 velocities show a good correlation with published velocities from the higher resolution study of Stauffer and Hartman (1986). The method 2 velocities have a dispersion of 19 km s^{-1} relative to the Stauffer and Hartman velocities, whereas the method 1 velocities show no correlation and a dispersion of 80 km s^{-1} . Thus *fitting to the narrow cross-correlation peak gives a more reliable velocity than fitting a template matched to the broader structure*. A preliminary report of this work was based on velocities measured by method 1 (Wade 1987). The resulting discussion in that report should in large part be disregarded.

In Figure 6 the Z Cha B velocity measurements obtained by cross-correlation with the Proxima Cen template are plotted as a function of orbital phase ϕ along with the fitted curve of a circular orbit,

$$V(\phi) = \gamma + K \sin 2\pi(\phi - \phi_0).$$

The binary phases are computed using the quadratic ephemeris given in Wood *et al.* (1986). From this weighted least-squares fit we find the orbital parameters $\gamma = -36 \pm 11 \text{ km s}^{-1}$, $K = 444 \pm 15 \text{ km s}^{-1}$, and $\phi_0 = -0.002 \pm 0.011$. The

rms residual to the fit is $\sigma = 71 \text{ km s}^{-1}$. The form 1σ uncertainties quoted here may be a bit too large, since the fit has a reduced χ^2/N of 0.72 with 44 degrees of freedom. The fitted values of K and γ have a correlation coefficient of +0.4 due to the higher density of measurements near phase 0.75 in comparison with phase 0.25.

To investigate possible systematic errors in the measured orbital parameters, we repeated the cross-correlation analysis with templates derived from each of the 19 M dwarf spectra. The fiducial phases obtained with different templates differ by only a small fraction of their uncertainties, and are all consistent with $\phi_0 = 0.00 \pm 0.010$. Different template spectra give significantly different γ velocities, and the velocities measured from the M dwarf spectra show a similar dependence on the template. We calibrated this small systematic effect by comparing the measured and published (Table 2) velocities of the M dwarf. The resulting "template corrections" range from -36 to $+34 \text{ km s}^{-1}$, and show no significant dependence on spectral type. After applying the template corrections, the M dwarf measurements have a dispersion relative to published velocities of 19 km s^{-1} . The corrected γ velocities range between -26 ± 12 and $-8 \pm 10 \text{ km s}^{-1}$, with a systematic trend from -23 km s^{-1} for late M templates to -10 km s^{-1} for early M templates. The γ velocity is systematically blueshifted with the early M templates because of the broad absorption feature on

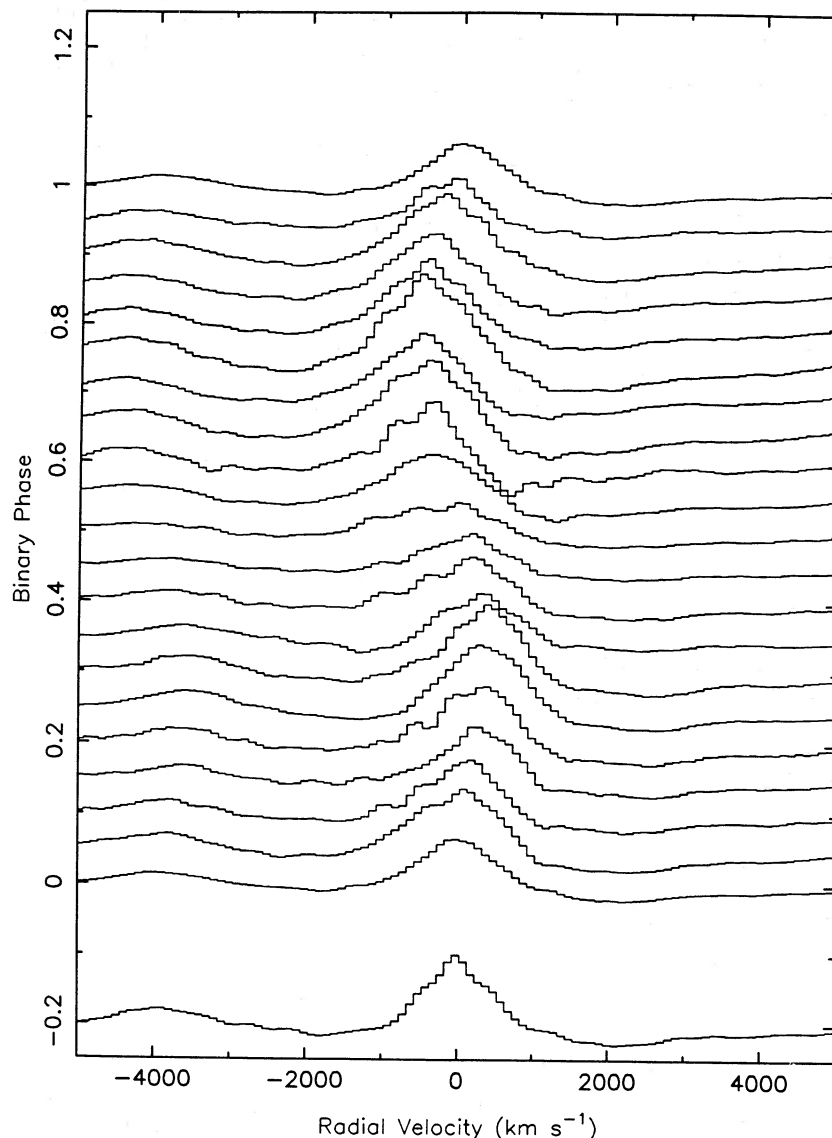


FIG. 5.—The autocorrelation function for the template spectrum of Proxima Cen (M5.5) and the cross-correlation of the template against a series of Z Cha spectra at 20 different binary phases. The orbital motion of Z Cha B causes the position of the cross-correlation peak to vary sinusoidally with binary phase over a full range of $\sim 900 \text{ km s}^{-1}$ (9 pixels). The peculiar shape of the autocorrelation function is caused by the doublet structure of the Na I line.

the red wing of the Na I doublet in Z Cha B (Fig. 2) and in other late M dwarfs (Fig. 3).

The K velocities obtained with different templates range between 439 and 458 km s^{-1} , and display a small systematic trend with spectral type, from 445 km s^{-1} for late M templates to 455 km s^{-1} for early M templates. The template corrections do not affect the K velocity. We prefer to use the results obtained with the late M templates, which most closely match the spectral type of Z Cha B, and accordingly adopt $\gamma = -23 \pm 15 \text{ km s}^{-1}$ and $K = 443 \pm 15$.

As a final check on the stability of the spectrograph and the appropriateness of our technique for radial velocity work, we measured the velocity of each of the Amiga spectra, using the average of all the Amiga spectra as a template. This velocity should be constant, and the velocity dispersion about the mean

was $\sim 13 \text{ km s}^{-1}$. Since the Amiga spectra were obtained strictly simultaneously with the spectra of Z Cha, and because the fiducial phase of the Na I radial velocity curve agrees with the expected phase of conjunction defined very accurately by the white dwarf eclipse, we are confident that we have an accurate *observed* value of K for Z Cha B.

The rotational broadening of the secondary star, assumed to be tidally locked with the binary orbit, is

$$V_{\text{rot}} \sin i = (K_1 + K_2)R_2/a \approx 0.462K_2 q^{1/3}(1+q)^{2/3},$$

where the final expression follows because the secondary star fills its Roche lobe ($q = M_2/M_1$). Thus an accurate measurement of the rotational broadening would provide a valuable independent check on the mass ratio of the binary (see, e.g., Gies and Bolton 1986). We unfortunately could not determine

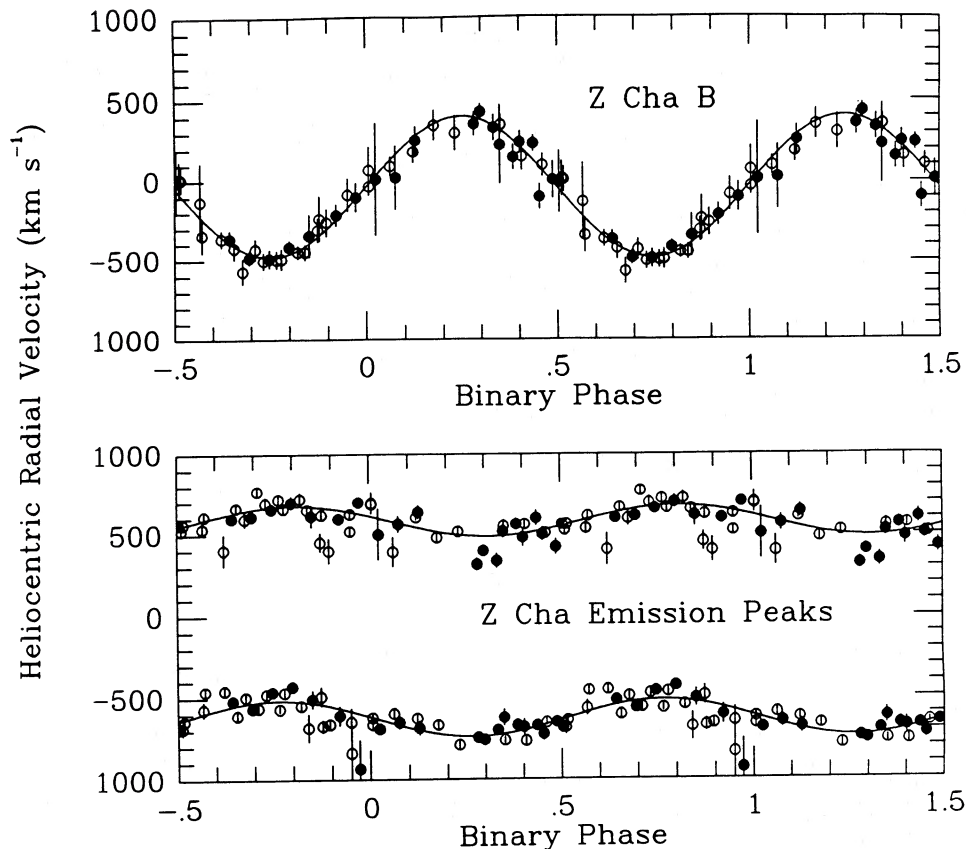


FIG. 6.—(top) Radial velocity curve for the secondary star Z Cha B, as measured from cross-correlation of the Na I doublet. (bottom) Radial velocity curves for the two peaks of the Ca II emission lines from the Z Cha accretion disk. Open and filled symbols represent data from different nights.

the rotational broadening of Z Cha B from our spectra because the CCD pixel size (100 km s^{-1}) and the Na I doublet splitting (400 km s^{-1}) were too large compared with the expected broadening of $\sim 100 \text{ km s}^{-1}$.

c) Slit-Photometric Light Curves

In this section we examine the continuum light curve of Z Cha and concurrent variations in the strengths of the TiO and Na I absorption features due to Z Cha B. The light curves are derived from our slit spectra, but are corrected for slit losses and sky transparency variations by using the simultaneously observed spectra of the Amiga, as described in § IIg. The relative photometry in these light curves should be good to $\sim 5\%$, although the absolute photometry is less certain because our “photometric” spectrum of the Amiga was obtained through thin cirrus clouds. We have adopted a normalizing factor that gives Z Cha Amiga a flux density of 3.5 mJy at $\lambda 7500$.

The light curve of Z Cha in the continuum band near $\lambda 7500$ is shown in Figure 7. The broad orbital hump centered at phase 0.8 and the narrow eclipse of the white dwarf and bright spot near phase 0.0 are clearly visible. Our time resolution is not sufficient to resolve the double-stepped shape of the eclipse. Comparison of this curve with, e.g., the broad-band white light curves of Wood *et al.* (1986) confirms that the correction for slit losses works as expected. The eclipse is shallower and the orbital hump is less prominent in our infrared data than in the white-light data of Wood *et al.* This is due to larger contributions from the secondary star and the outer parts of the ac-

culation disk, relative to the white dwarf and bright spot, at $\lambda 7500$ than in the white-light bandpass ($\lambda_{\text{eff}} \approx 5000 \text{ \AA}$).

Figure 8 displays the orbital variations of the flux density deficits in the TiO bands at $\lambda 7165$ and $\lambda 7665$ relative to the linear continuum defined in § IIIa. The TiO $\lambda 7665$ curve is also shown in Figure 7 for comparison with the continuum light curve. The TiO deficit light curves reflect the behavior of Z Cha B only, since the white dwarf, bright spot, and accretion disk should not produce significant TiO bands.

The TiO light curves have roughly equal maxima near the two quadrature phases, and unequal minima near the conjunctions. Thus weaker TiO absorption is seen near $\phi = 0.5$, when we view the “pointed” side of Z Cha B, than near $\phi = 0$, when we view the “back” side facing away from the white dwarf. Throughout the orbit the TiO band ratio is consistent with a value of 1.5, similar to M5.5 dwarf stars (see Fig. 4).

Figure 9 compares the TiO light curve, now integrated over a wider bandwidth to increase the signal-to-noise ratio, with the light curve of the Na I doublet. The Na I light curve is noisier but presents qualitatively the same features as TiO, in particular the broad decline in the absorption strength around $\phi = 0.5$.

The persistence of the TiO and Na I absorption during the narrow primary eclipse confirms that these features arise from Z Cha B. The larger projected area of the Roche lobe at quadrature phases provides a natural explanation for the increased absorption deficits seen at the quadratures. These “ellipsoidal variations” are not evident in the continuum light curve

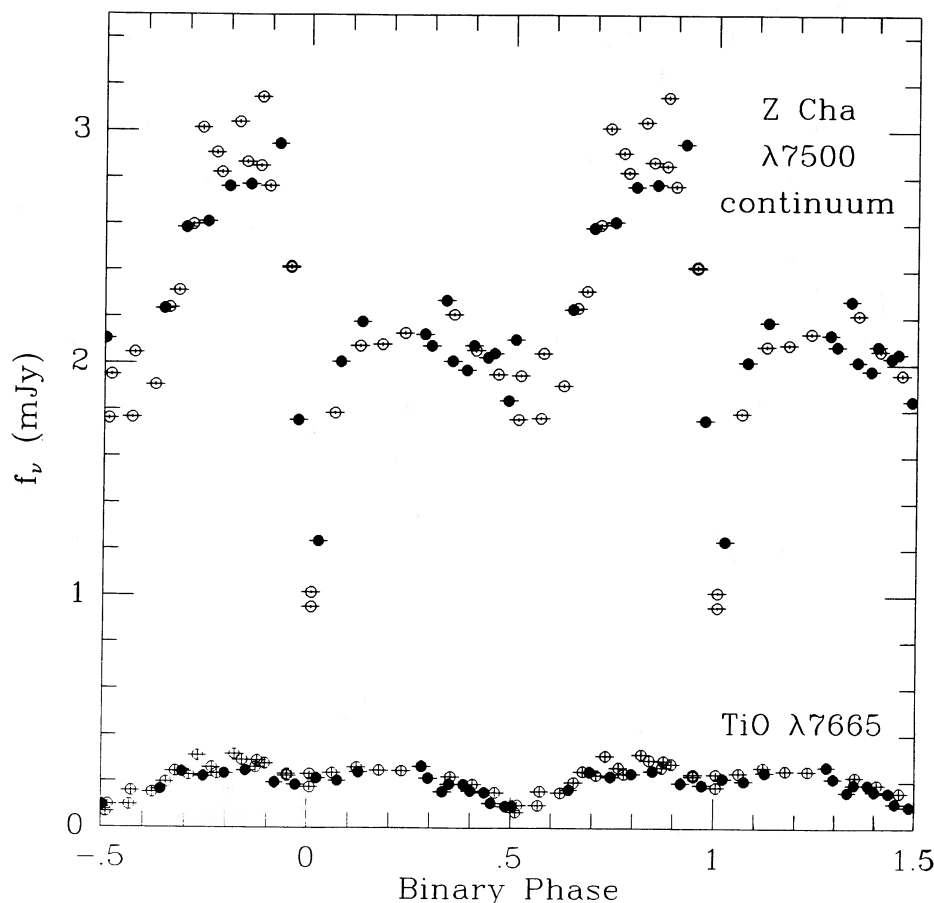


FIG. 7.—The continuum light curve of Z Cha showing the broad orbital hump centered at phase 0.8 and eclipse of the white dwarf, bright spot, and accretion disk by the secondary star at phase 0.0. The light curve of the TiO $\lambda 7665$ flux density deficit is shown on the same flux scale for comparison. Open and filled symbols represent data from different nights.

because Z Cha B contributes only $\sim 15\%$ of the $\lambda 7500$ light. The ellipsoidal variations are more prominent farther into the infrared, with an observed depth of ~ 0.25 mag at J ($1.25 \mu\text{m}$) and K ($2.2 \mu\text{m}$) where Z Cha B contributes over half of the system's light (Bailey *et al.* 1981).

Geometric factors are not the sole cause of the TiO and Na I variations, however, because the primary and secondary minima would then have nearly equal depths as illustrated by the model light curves in Figure 9 and discussed further in § IVa below. The observed TiO light curve has a primary (i.e., $\phi = 0.0$) minimum ~ 0.2 mag deep, but the depth of the secondary minimum is over a magnitude.

IV. DISCUSSION

a) Modeling the TiO Distribution of Z Chamaeleontis B

The TiO and Na I flux deficit light curves presented in Figures 8 and 9 result both from changes in the projected surface area of Z Cha B as it rotates in synchronism with the binary orbit and from variations of the absorption strengths over the stellar surface. The surface variations arise because the structure of the cool stellar atmosphere depends on the local surface temperature, surface gravity, and external irradiation. The nonuniform line strength also affects our interpretation of the radial velocity curve measured from Na I; we derive a correction for this in § IVb.

To interpret the observed flux deficit variations, we developed a computer model to synthesize light curves and radial velocity curves. The model uses the Roche geometry to describe the tidal and rotational distortion of the stellar surface and the associated variations in the local surface gravity. Z Cha B is assumed to fill its Roche lobe exactly. We adopt a mass ratio $q = M_2/M_1 = 0.1495$, inclination $i = 81^\circ 7'$, separation $a = 0.634 R_\odot$, and distance $d = 100$ pc, from the results of Wood *et al.* (1986).

We first consider whether the observed light curves can be accounted for purely in terms of limb-darkening and gravity-darkening effects. Gravity darkening is treated according to Von Zeipel's law,

$$T_{\text{eff}}^4 \propto g^\beta,$$

where T_{eff} is the local effective temperature, g is the local surface gravity, and β is the gravity-darkening index ($\beta = 0.08$ for late-type stars with convective envelopes). The local continuum intensity is given by

$$I_v(\lambda, \theta) = B_v(\lambda, T_{\text{eff}}) \frac{1 - u + u \cos \theta}{1 - (u/3)},$$

where B_v is the Planck function, u is the linear limb-darkening coefficient, and θ is the angle between the observer's line of sight and the local vector normal to the stellar surface.

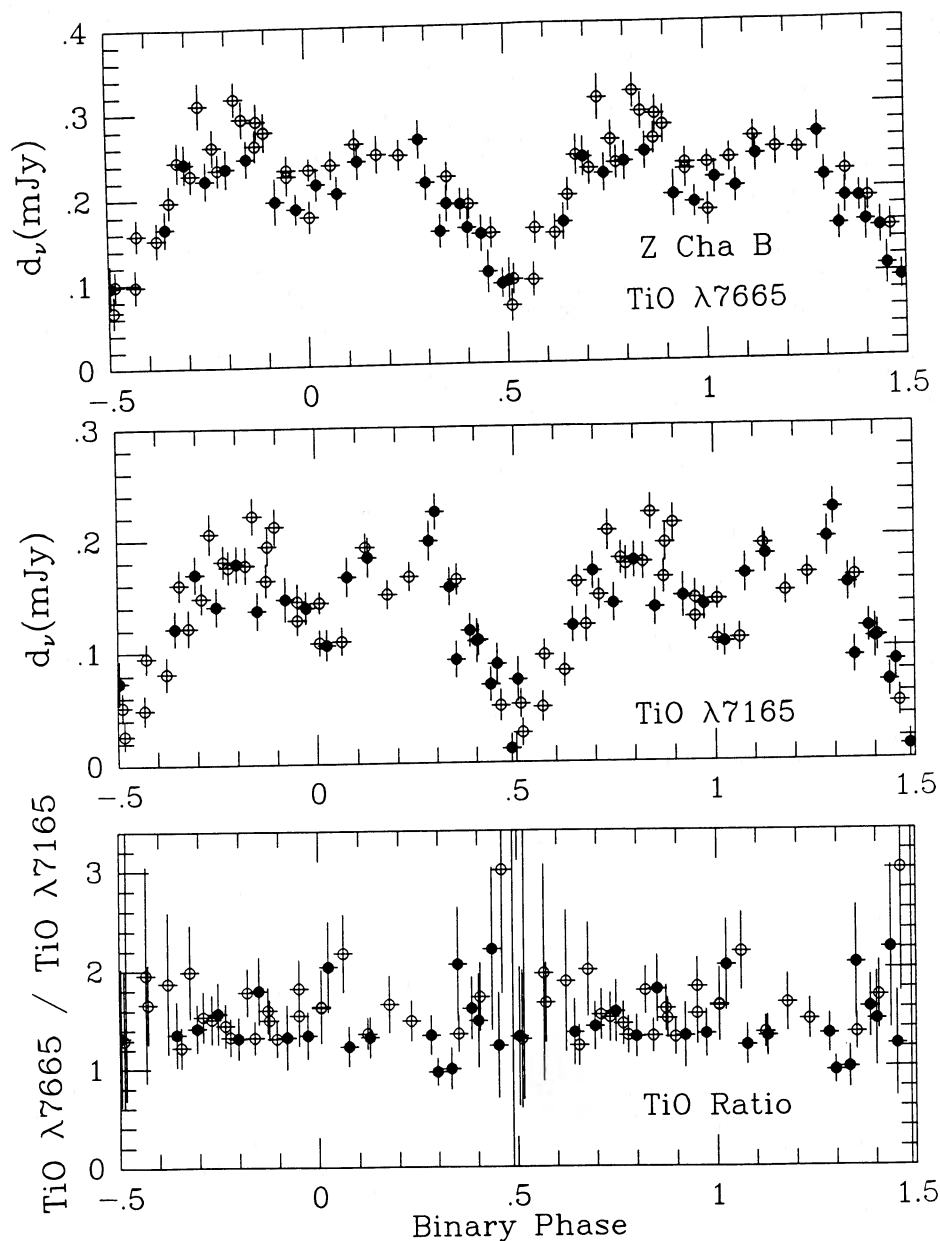


FIG. 8.—The variation with binary phase of the TiO absorption bands, measured at $\lambda 7165$ and $\lambda 7665$ relative to a linear continuum fitted at $\lambda 7500$ and $\lambda 8200$. These give a light curve of Z Cha B in the light of the TiO band strength. The TiO band ratio is also shown. The band ratio falls off-scale for two points with larger error bars near phase 0.5. Open and filled symbols represent data from different nights.

To complete the model, we need to describe how the equivalent widths of the absorption features depend on T_{eff} and on θ . From Figure 3, it is clear that the TiO and Na I equivalent widths are smaller for earlier spectral types, but the precise connection between T_{eff} and spectral type is somewhat uncertain. We would also expect reduced equivalent widths to occur near the limb of the star, although this depends on details of the vertical structure in the upper layers of the cool stellar atmosphere. In light of these uncertainties, we chose to consider models with a constant equivalent width, since the T_{eff} and θ dependences can be represented approximately by appropriate changes in β and u , respectively.

Synthetic light curves for $u = 0.5$ and $\beta = 0.08$ are superposed on the data in Figure 9. This model predicts a primary

minimum that is too deep, and a secondary minimum that is too shallow relative to the observations. We tried many different combinations of u and β , but found that both minima become deeper when either u or β is increased. Thus no combination of limb-darkening or gravity-darkening parameters can satisfactorily fit the data.

If the outer accretion disk is optically thick at $\lambda 7500$, then the partial eclipse of Z Cha B by the accretion disk could increase the depth of the secondary minimum without affecting the primary minimum. We adopt a disk radius $R_D = 0.334a$ (Wood *et al.* 1986) and a constant opening angle $H/R = 0.05$, where $2H$ is the thickness of the disk at radius R . In Figure 9 the synthetic light curves including the secondary eclipse show that the data still cannot be satisfactorily reproduced because

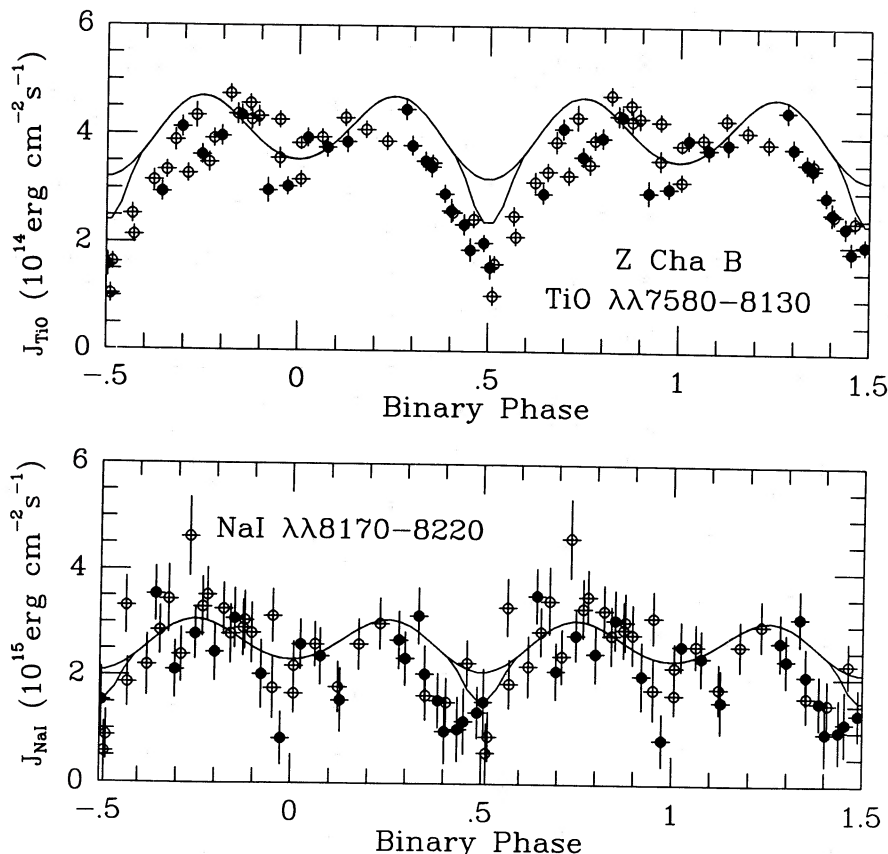


FIG. 9.—The integrated absorption flux deficit in the TiO band between $\lambda\lambda 7580$ and 8130 and in the Na I absorption doublet. The similar phase variations suggest that TiO and Na I have similar distributions over the surface of Z Cha B. Open and filled symbols represent data from different nights. The models used to compute the synthetic light curves assume a Roche-lobe filling secondary star with gravity-darkening index $\beta = 0.08$, corresponding to a convective envelope, and limb-darkening coefficient $u = 0.5$. If the accretion disk is optically thick, it may partially eclipse the secondary star, producing the narrow minimum at phase 0.5. The observed light curve has a deeper and broader minimum near phase 0.5 than the synthetic light curves.

the secondary eclipse is confined to a relatively narrow phase range around secondary minimum.

Finally, we consider the effect of irradiation. An indication of the importance of irradiation in Z Cha can be obtained by comparing rough estimates for the internal flux from Z Cha B,

$$F_{\text{int}} \approx \sigma T_2^4,$$

and for the flux incident on Z Cha B from the hot white dwarf,

$$F_{\text{irr}} \approx \sigma T_1^4 (R_1/a)^2.$$

Estimating the secondary star temperature T_2 from the M5.5 spectral type, and taking the separation a , white dwarf temperature T_1 , and radius R_1 from Wood *et al.* (1986), we find

$$\frac{F_{\text{irr}}}{F_{\text{int}}} \approx \left(\frac{T_1}{T_2}\right)^4 \left(\frac{R_1}{a}\right)^2 \approx \left(\frac{12,000}{2700}\right)^4 \left(\frac{0.0125}{0.634}\right)^2 \approx 0.15.$$

A similar calculation indicates that the bright spot at the outer rim of the accretion disk produces a dose of irradiation similar to that from the white dwarf. Thus irradiation effects may be observable but are probably not a dominant source of heat on the surface of Z Cha B.

According to the standard treatment of reflection effects in interacting binary stars, irradiation elevates the local effective temperature to produce a total outward flux equal to the unperturbed internal flux plus a fraction of the incident flux,

$$\sigma T_{\text{eff}}^4 = W F_{\text{irr}} + F_{\text{int}},$$

where σ is the Stefan-Boltzmann constant and the albedo W is the fraction of the incident flux that is thermalized (see, e.g., Hessman *et al.* 1984). In our model we assume that the incident flux originates from a point source at the position of the white dwarf, and we allow for the finite thickness of the accretion disk, which shields the equatorial regions of Z Cha B from the irradiation.

Irradiation would appear to offer a natural explanation for the diminished absorption features at phase 0.5, when we view the irradiated side of Z Cha B, since the TiO and Na I equivalent widths decrease with increasing effective temperature (see Fig. 3). However, the empirical relationship between surface brightness and $V-R$ index (e.g., Barnes and Evans 1976; Popper 1980) indicates that the continuum surface brightness increases even more rapidly with temperature than the absorption equivalent widths fall. Thus the TiO and Na I flux deficits should actually *increase* as the effective temperature is elevated by irradiation. This prediction is just the opposite of what we observe in Z Cha.

The standard treatment of reflection effects thus appears to be incorrect for modeling the behavior of the TiO absorption features. The spectrum that emerges from the irradiated surface does not simply mimic that of an isolated star with a higher temperature. We suspect that the irradiation substantially modifies the vertical structure of the atmosphere of Z Cha B. TiO bands might be suppressed if the atmospheric temperature gradient is reduced or inverted as a result of the deposition of

heat near and above the photosphere. Further exploration of this interesting possibility would require a grid of cool irradiated model atmospheres covering a range of gravity, temperature, and irradiation.

b) The “K-Correction”

Hessman *et al.* (1984) reported large systematic changes in the K velocity of the secondary star in the dwarf nova SS Cygni, from 155 km s^{-1} in quiescence to 210 km s^{-1} in outburst. They attribute this change in the K velocity to a quenching of the absorption lines on the side of the secondary star that is heated by irradiation from the accretion disk. The non-uniform absorption distribution distorts the rotationally broadened line profile and gives rise to a systematic velocity shift at each binary phase. Consequently, the observed radial velocity curve is not exactly sinusoidal, and the measured value for K_2 , obtained by fitting a sine curve to the observed velocities, is different from the true (dynamical) value. Hessman *et al.* did not directly measure line strengths variations in SS Cygni, but their interpretation is appealing, and it seems likely that irradiation can alter K velocities in other systems. Our spectrophotometric data show directly that the TiO and Na I absorption distribution is very uneven on the surface of Z Cha B. Our measured value of K_2 must be corrected for this effect.

A rough estimate of this “K-correction” is obtained by assuming that the “effective center” of Z Cha B, weighted by the strength of the absorption lines, is displaced from the center of mass of the star in the direction away from the white dwarf. The size of this displacement is

$$\Delta R = f R_2,$$

where R_2 is the radius of Z Cha B and $|f|$ is less than unity. The center of mass of Z Cha B lies at a distance

$$a_2 = \frac{a}{1+q}$$

from the center of mass of the binary, where $q = M_2/M_1$ is the mass ratio and a is the separation between the binary components. The “effective center” of Z Cha B lies at $a_2 + \Delta R$ from the center of mass of the binary. Therefore the observed amplitude of the velocity variation, K_{obs} , is larger than the true (dynamical) amplitude, K_2 , by an amount

$$\Delta K = \frac{\Delta R}{a_2} K_2.$$

With $q = 0.15$ from Wood *et al.* (1986), we find $R_2 = 0.23a$ and $a_2 = 0.87a$, so that

$$\Delta K = 0.27fK_2$$

or

$$K_2 = K_{\text{obs}}/(1 + 0.27f).$$

As an extreme case suppose that the back hemisphere of the star has a uniform absorption line strength and the front hemisphere has no absorption at all. Then $f = 4/3\pi \approx 0.42$, and the correction to K_{obs} is $\sim 11\%$, or $\sim 45 \text{ km s}^{-1}$. Note that masses derived from the uncorrected K velocity could thus be in error by as much as $\sim 30\%$.

To obtain a more accurate K-correction, we need to determine the Na I distribution on the surface of Z Cha B. The results from Figure 9 indicate that Na I and TiO are both weaker on the side of Z Cha B that faces the white dwarf than

on the opposite side. Although we are not certain of the physical explanation for this effect, we can use the observed light curves to determine empirically the distribution of the absorption features. We assume that the Na I and TiO distributions are similar, so that the higher quality TiO flux deficit curves can be used to constrain the distribution.

None of the physical models we considered in § IIIa could reproduce the observed decrease in the TiO flux deficit near phase 0.5. However, an acceptable fit can be obtained with an ad hoc modification in which the absorption is artificially set to zero in a region around the L_1 point. In this one-spot model, the absorption-free region around the L_1 point is defined by $\{X < X_{\text{limit}}\}$, where the Cartesian coordinate X is 0 at the white dwarf, and 1 at the center of mass of Z Cha B. The parameter X_{limit} thus controls the size of the absorption-free region, which can be zero if $X_{\text{limit}} < X_{L_1} \approx 0.69$, or can cover an entire hemisphere of Z Cha B if $X_{\text{limit}} = 1.0$.

Figure 10 (*top*) illustrates the range of light curves possible with the one-spot model as the absorption-free region around the L_1 point is increased through $X_{\text{limit}} = 0, 0.8, 0.9, 1.0$. As before, we use a gravity-darkening parameter $\beta = 0.08$ and limb-darkening coefficient $u = 0.5$. Synthetic light curves are shown both with and without a secondary eclipse at phase 0.5. The best fit to the data is obtained for $X_{\text{limit}} = 0.88$ with the secondary eclipse, or 0.87 without the eclipse.

We synthesized velocity curves for each of these models by computing at each phase the average radial velocity over the visible surface of Z Cha B, weighted by the local line strength. The synthetic velocity curves are slightly nonsinusoidal, showing a positive velocity residual just before superior conjunction of Z Cha B ($\phi = 0.5$) and a corresponding negative velocity residual just after superior conjunction. It is this deviation from a sine curve that ultimately gives rise to ΔK . (Thus the treatment of the distortions as just a displacement of an “effective center” is only approximate.) The K-correction, found by fitting a sinusoid to the synthetic velocity curves, is $K_2/K_{\text{obs}} = 1.003, 0.983, 0.935, 0.860$ for the $X_{\text{limit}} = 0, 0.8, 0.9, 1.0$ models respectively. The K-correction is not sensitive to the presence or absence of a secondary eclipse because the radial velocity is close to zero at conjunction. The K-correction for the one-spot models most closely fitting the observed TiO light curve is $K_2/K_{\text{obs}} = 0.967 \pm 0.005$.

The one-spot models are extreme in the sense that they have an infinite contrast between the absorption strength on opposite sides of Z Cha B. An extreme model in the opposite sense can be found by applying the maximum-entropy method (Skilling and Bryan 1984), which generates the “most uniform” distribution that is consistent with the observed flux deficit curves. We fitted our synthetic light curves to the observations by using the maximum-entropy fitting program MEMSYS (Skilling and Bryan 1984) to adjust the TiO distribution, which was assumed to be symmetric about the equatorial plane. Synthetic light curves for maximum-entropy models with and without a secondary eclipse are compared with the observations in Figure 10 (*bottom*). With the freedom to adjust the entire distribution, the maximum-entropy method achieved a better fit to the observations, $\chi^2/N \approx 4$, than was possible with the parameterized one-spot models. The maximum-entropy TiO distribution with no secondary eclipse has a minimum at the L_1 point and rises smoothly to a level 3 times higher on the hemisphere facing away from the white dwarf. The K-correction for this distribution is $K_2/K_{\text{obs}} = 0.979$. When the secondary eclipse is included, the

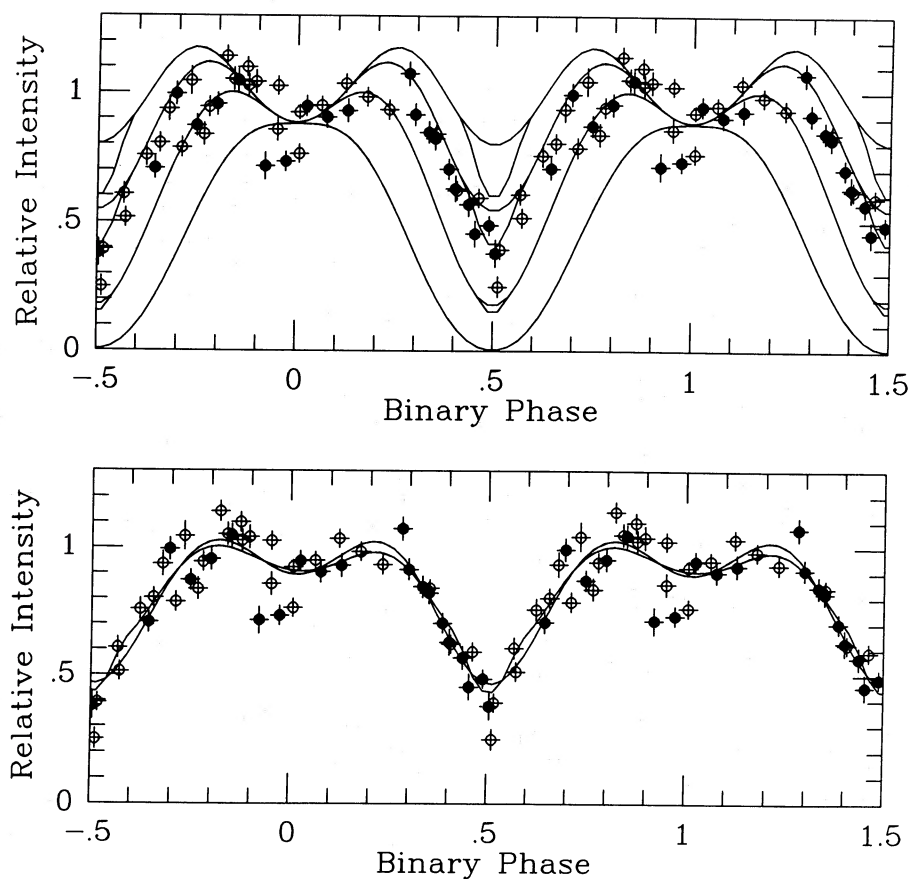


FIG. 10.—Synthetic light curves are compared with the observed variations in the TiO absorption flux deficit. The effect of setting the TiO absorption to zero in a progressively larger region around the inner Lagrangian point is illustrated in the top portion; the lowest curve corresponds to the largest zero-absorption region. In the bottom portion, the TiO distribution on the surface of the secondary star was fitted to the data by the maximum entropy method, with and without considering the effect of an eclipse by the accretion disk.

contrast is reduced to a factor of 2, and the K -correction becomes 0.984.

The true absorption distribution on the surface of Z Cha B probably lies somewhere in between the one-spot and maximum-entropy models. The K -correction factor should therefore be somewhere between 0.96 and 0.98. Combining the measure semiamplitude $K_{\text{obs}} = 443 \pm 15 \text{ km s}^{-1}$ with the correction of $-13 \pm 4 \text{ km s}^{-1}$, we arrive at an estimate of $K_2 = 430 \pm 16 \text{ km s}^{-1}$ for the true motion of Z Cha B.

c) Physical Parameters of Z Chamaeleontis

As one of the few eclipsing, double-lined spectroscopic binaries among the cataclysmic variables, Z Cha offers redundant observational constraints on any dynamical model. In addition to the orbital period, P , these constraints are: the radial velocity semiamplitudes of the two stellar components K_1 and K_2 , the white dwarf eclipse width $\Delta\phi(\text{wd})$ and ingress width $\Delta(\text{wd})$, the ingress and egress phases of the bright spot eclipse $\phi_i(\text{bs})$ and $\phi_e(\text{bs})$, and two measurements from the emission lines that arise in the accretion disk, the largest velocity in the wings of the profile V_{max} and the velocity splitting between the peaks of the emission line $2V_{\text{min}}$. We show below that these constraints do not yield a consistent model for Z Cha unless standard assumptions are relaxed.

The parameters that describe a model of Z Cha are the stellar masses M_1 and M_2 and radii R_1 and R_2 , the orbital

inclination i and separation a , and the bright spot radius R_{bs} from the center of the disk to the bright spot on its outer rim. Under standard assumptions (see, e.g., Wade 1985), the secondary star radius $R_2(a, q)$ is defined by the condition that it fills its Roche lobe (Eggleton 1983). Here $q = M_2/M_1$ is the mass ratio. The separation, of course, follows from the masses and the binary period, $P = 0.074499$ days.

Cook and Warner (1984) developed a method of solving for the mass ratio q and the normalized bright spot radius R_{bs}/a from the observed contact phases of the bright spot eclipse, $\phi_i(\text{bs})$ and $\phi_e(\text{bs})$. This method assumes that the gas stream from the inner Lagrangian point to the bright spot on the outer rim of the disk follows a ballistic trajectory, which is sensitive to q . At the same time, the mass ratio q and inclination i must be chosen in accordance with the observed phase width of the white dwarf eclipse, $\Delta\phi(\text{wd}) = 19^\circ 3' \pm 0^\circ 1'$ (Bailey 1979; Wood *et al.* 1986). Thus observations of the white dwarf and bright spot eclipses together result in a unique combination of q and i , along with dimensionless sizes for the disk and the secondary star. An absolute linear size for the system, and hence the stellar masses, follows from the assumptions that the duration of primary ingress $\Delta(\text{wd})$ measures the dimensionless size of the white dwarf and that the absolute radius of the primary is given by the relation $R_{\text{wd}}(M_1)$ for white dwarfs (e.g., Hamada and Salpeter 1961). Alternatively, the linear size follows from the assumption that the secondary star obeys a particular

mass-radius relation, e.g., a ZAMS relation, or more traditionally from measuring the size of the orbit via K_1 or K_2 .

It is thus possible to solve for the Z Cha system parameters in several different ways. We now discuss four different models of the Z Cha binary, which are presented in order of ascending white dwarf mass in the first part of Table 4. The second part of the table confronts each model's predictions with the observational constraints. The predicted values of $2V_{\min}$ and $2V_{\max}$ assume that the emission lines originate throughout the disk, i.e., from the surface of the central star to the bright spot radius, and are shaped by the Keplerian motion of the gas around the white dwarf.

Model P, following Wood *et al.* (1986), relies entirely on photometric observations. The white dwarf eclipse width $\Delta\phi(\text{wd})$ and the bright spot eclipse timings $\phi_i(\text{bs})$ and $\phi_e(\text{bs})$ determine the mass ratio q , the inclination i , and the disk radius R_{bs}/a . The white dwarf ingress width $\Delta(\text{wd})$ then provides a photometric measurement of the white dwarf radius R_1/a , which in combination with the Hamada-Salpeter (1961) mass-radius relation establishes a length scale in the binary system. The corresponding stellar masses are $M_1 = 0.555 M_\odot$ and $M_2 = 0.083 M_\odot$.²

Model K uses the length scale established in this study by following Z Cha B in its orbit: it is based on our measurement of K_2 . The mass function corresponding to the measured value of $K_2 = 430 \pm 16 \text{ km s}^{-1}$ is

$$\frac{PK_2^3}{2\pi G} = \frac{M_1 \sin^3 i}{(1+q)^2} = 0.62 \pm 0.07 M_\odot.$$

If the mass ratio were smaller than 0.06, the Roche lobe of the secondary star would be too small to produce the observed width of the primary eclipse. Thus with $i = 90^\circ$ and $q = 0.06$ the mass function gives a strict lower bound to the white dwarf mass, $M_1 > 0.70 \pm 0.08 M_\odot$. As in model P, model K adopts values for q , i , and R_{bs} that fit the white dwarf and bright spot eclipse timings. The resulting masses are $M_1 = 0.84 \pm 0.09 M_\odot$ and $M_2 = 0.125 \pm 0.014 M_\odot$, with $1 - \sigma$ uncertainties that are dominated by the uncertainty in K_2 .

Model S is a traditional spectroscopic solution, which employs a spectroscopic estimate of the mass ratio,

$$q = \frac{K_1}{K_2} = \frac{88 \pm 8}{430 \pm 16} = 0.20 \pm 0.02.$$

Here $K_1 = 88 \pm 8 \text{ km s}^{-1}$ is the semiamplitude of the radial velocity curve for the wings of the emission lines, as measured by Marsh, Horne, and Shipman (1987). This spectroscopic mass ratio is significantly larger than the photometric mass ratio obtained from the bright spot eclipse timings. Thus model S cannot fit the two bright spot eclipse timings simultaneously. The disk radius can be adjusted to fit the bright spot egress phase $\phi_e(\text{bs})$, as in Table 4, but the predicted value of $\phi_i(\text{bs})$ then departs from the observed value by $\sim 30 \sigma$. To obtain the spectroscopic mass ratio, one must assume that the apparent orbital motion of emission lines from the accretion disk is identical to that of the white dwarf. This interpretation may be incorrect, however, because the phase of the emission-line radial velocity curve is shifted by $+18^\circ \pm 5^\circ$ relative to the white dwarf eclipse. Still larger phase shifts are observed in

other systems. As discussed by Marsh, Horne, and Shipman (1987), a small eccentricity of the streamlines or a brightness asymmetry in the disk can account for the phase shift and spurious K velocity of the emission lines.

Model M, following Cook and Warner (1984), forces the secondary star to lie on the zero-age main sequence as defined by Lacy (1977). Cook and Warner (1984) adopted a similar high-mass model of Z Cha with $M_1 \approx 1.3$ and $M_2 \approx 0.2$, the difference lying only in the specific form adopted for the main-sequence mass-radius relation. We note that the main-sequence relation is not well determined empirically for such low-mass stars, relying for most of its weight on only two eclipsing binary systems, CM Dra and YY Gem (see Lacy 1977). Furthermore, "the" lower main-sequence mass-radius relation may have a finite thickness due to differences in chemical composition and age. Finally, one has reason to expect (e.g., Paczyński and Sienkiewicz 1981) that the secondary stars in low-mass cataclysmic binaries should be somewhat distended as the result of relatively rapid mass loss (see below). For neither the Cook and Warner masses nor those presented as model M (based on the Lacy 1977 relation) is the observed value of K_2 reproduced.

As inspection of Table 4 and the above discussion show, the standard model does not permit all of the observational constraints to be satisfied simultaneously, so the table also lists *extra parameters*, indicating where assumptions can be relaxed to improve agreement with the data. Thus in the third part of Table 4, $R_1/R_{\text{wd}}(M_1)$ permits the primary star to be larger than a Hamada-Salpeter white dwarf, R_{\min}/R_1 permits the emission-line region of the accretion disk to begin at a radius larger than that of the primary star, and R_{\max}/R_{bs} permits the accretion disk emission-line region to extend outside the bright spot position. (The ratio of observed to predicted V_{\min} is also tabulated.) These extensions allow observations of the white dwarf eclipse width, the bright spot ingress, and the emission-line velocities to be accommodated. The final section of Table 4 repeats for convenience the observational constraints which are not satisfied, even with the extension of the standard model. If K_1 is disregarded, model K can be made to satisfy all constraints, and in the discussion that follows, we adopt model K as the "preferred" solution and compare the other models with it.

The measured value of $K_2 = 430 \pm 16$ is larger by 3σ than the value of $K_2 = 375 \pm 3 \text{ km s}^{-1}$ predicted by Wood *et al.* (model P), and the spectroscopic masses of model K are therefore larger by the factor $(430/375)^3$. It also follows that the radius of the primary star is forced to be $50\% \pm 15\%$ larger than the Hamada-Salpeter radius $R_{\text{wd}}(M_1)$ corresponding to the spectroscopic mass M_1 , if the measured phase angle $\Delta(\text{wd}) = 3^\circ 0' \pm 0^\circ 1'$ during which it disappears behind the secondary star is to be correctly predicted. Similar large changes of $R_1/R_{\text{wd}}(M_1)$ from unity are required by models S and M, as shown in Table 4.

One may ask whether relaxing (1) the assumption that the Hamada-Salpeter rule correctly relates the mass and radius of the central star and/or (2) the assumption that the ingress duration of primary eclipse measures the size of the white dwarf, can allow the photometric and spectroscopic masses to be reconciled. With regard to (1), the Wood *et al.* masses are based on the Hamada-Salpeter (1961) mass-radius relation for cold degenerate matter of pure carbon composition. Allowance for a small increase in the white dwarf radius due to nonzero temperature and a low-mass envelope of hydrogen or helium

² These revised parameters from Wood (1986) differ slightly from those reported by Wood *et al.* (1986) due to a small numerical error in the Monte Carlo routine described in Wood *et al.* The error estimates are essentially unchanged.

TABLE 4
OBSERVED CONSTRAINTS AND MODELS^a OF THE Z CHAMAELEONTIS BINARY

A. Parameters ^b for Standard Assumptions						
PARAMETER	MODELS				REFERENCES	
	P	K	S	M		
$M_1(M_\odot)$	0.555	0.836	0.934	1.164		
$M_2(M_\odot)$	0.083	0.125	0.191	0.174		
q	0.1495	0.1495	0.204	0.1495		
i	81°78	81°78	80°04	81°78		
$a(R_\odot)$	0.641	0.735	0.775	0.821		
R_{bs}/a	0.334	0.334	0.327	0.334		
$R_2(a, q)R_\odot$	0.150	0.172	0.197	0.192	1	
$R_{ZAMS}(M_2)R_\odot$	0.097	0.142	0.209	0.192	2	
$R_{wd}(M_1)R_\odot$	0.0125	0.0094	0.0084	0.0060	3	
B. Predicted and Observed Constraints ^c						
CONSTRAINT	PREDICTED				OBSERVED	REFERENCES
	P	K	S	M		
$\Delta\phi(\text{wd})$	19°3	19°3	19°3	19°3	$19°3 \pm 0°1$	4, 5
$\Delta(\text{wd})$	3°0	2°0	1°8	1°1	$3°0 \pm 0°1$	4, 5
$\phi_i(\text{bs})$	-4°3	-4°3	-6°7	-4°3	$-4°3 \pm 0°1$	4, 5
$\phi_e(\text{bs})$	28°3	28°3	28°3	28°3	$28°3 \pm 0°1$	4, 5
K_2 (km s ⁻¹)	375	430	430	480	430 ± 16	6
K_1 (km s ⁻¹)	56	64	88	72	88 ± 8	7
$2V_{\min}$ (km s ⁻¹) ...	1390	1600	1650	1780	1200 ± 50	6, 7
$2V_{\max}$ (km s ⁻¹) ...	5750	8140	9090	12100	4200 ± 100	6, 7
C. Extra Parameters ^b Extending Standard Assumptions						
PARAMETER	MODELS					
	P	K	S	M		
$R_1/R_{wd}(M_1)$	1.0	1.5	1.6	2.7		
R_{\min}/R_1	1.9	2.5	2.9	3.1		
R_{\max}/R_{bs}	1.3	1.8	1.9	2.2		
$V_{\min}/(V_{\text{kep}} \sin i)$...	0.86	0.75	0.73	0.67		
D. Predicted and Observed Constraints ^c Still Not Satisfied						
CONSTRAINT	PREDICTED				OBSERVED	REFERENCES
	P	K	S	M		
$\phi_i(\text{bs})$	-4°3	-4°3	-6°7	-4°3	$-4°3 \pm 0°1$	4, 5
K_2 (km s ⁻¹)	375	430	430	480	430 ± 16	6
K_1 (km s ⁻¹)	56	64	88	72	88 ± 8	7

^a MODELS.—P: photometric model, following Wood *et al.* 1986, with q , i , and R_1 from eclipse timings and M_1 from the Hamada and Salpeter 1961 white dwarf mass-radius relationship, predicts K_2 too small. K: preferred model based on K_2 from this work, with q and i from eclipse timings. S: traditional spectroscopic model, with mass ratio $q = K_1/K_2$, inconsistent with bright spot eclipse constraints. M: model with secondary star on the Lacy 1977 zero-age main sequence, predicts K_2 too large.

^b PARAMETERS.— M_1 , M_2 = masses of primary and secondary stars; $q = M_2/M_1$; i = inclination; a = separation; R_{bs} = radius of bright spot from center of disk; R_1 = radius of primary star; $R_2(a, q)$ = radius of secondary star from volume of Roche lobe; $R_{wd}(M_1)$ = radius of Hamada and Salpeter 1961 white dwarf; $R_{ZAMS}(M_2)$ = radius of Lacy 1977 zero-age main-sequence star; R_{\min} , R_{\max} = inner and outer radius of accretion disk emission line region; $V_{\text{kep}} = (GM_1/R_{bs})^{1/2}$.

^c CONSTRAINTS.— $P = 0.074499$ days = binary period; $\Delta\phi(\text{wd})$ = duration of white dwarf eclipse; $\Delta(\text{wd})$ = duration of white dwarf ingress; $\phi_i(\text{bs})$, $\phi_e(\text{bs})$ = ingress and egress of bright spot; K_1 , K_2 = semiamplitude of radial velocity curves; V_{\min} , V_{\max} = velocity at peak and extreme wings of emission lines.

REFERENCES.—(1) Eggleton 1983; (2) Lacy 1977; (3) Hamada and Salpeter 1961; (4) Cook and Warner 1984; (5) Wood *et al.* 1986; (6) this work; (7) Marsh, Horne, and Shipman 1987.

(see, e.g., Koester and Schoenberger 1986) would increase the inferred (photometric) mass by a small amount:

$$\Delta(\log M_1) = \frac{3}{1 + 3\alpha} \Delta(\log R_1),$$

where

$$\alpha = -\frac{d(\log R)}{d(\log M)}$$

is the power-law index of the mass-radius relation ($\alpha \approx 0.7$ for $M_1 \approx 0.7 M_\odot$). However, as the white dwarf surface temperature is $\sim 10^4$ K (Wood *et al.* 1986; Marsh, Horne, and Shipman 1987), the radius can be increased by only $\sim 5\%$. Thus this effect alone is not large enough to reconcile the spectroscopic and photometric results. With regard to (2), the photometric method gives, strictly speaking, an upper limit to the radius of the primary star and a lower limit to the masses, since a suitable brightness distribution in the inner region of the accretion disk can in principle mimic a star with a larger radius (Cook and Warner 1984; Wood *et al.* 1986). However, radius measurements on different eclipse cycles have an rms scatter of only 10% in the Wood *et al.* data, and the radii determined independently by Cook and Warner (1984) and Wood *et al.* (1986) agree to similar precision. Also, the detailed shape of the white dwarf ingress and egress light curves does not support the existence of a bright equatorial boundary layer or a bright inner disk (Wood 1986). Thus the available evidence suggests a *spherically symmetric central object with a definite radius*. Closer scrutiny of the light curves and high time resolution spectroscopy is needed to establish the central object's true nature.

The emission lines that arise from the accretion disk provide two additional constraints on the white dwarf mass, which under the standard assumptions are violated by all four models of Table 4. The largest velocity in the wings of the emission line profile is $V_{\max} = 2100 \pm 50 \text{ km s}^{-1}$ (Marsh, Horne, and Shipman 1987). Comparison with the projected Keplerian velocity at the inner edge of the accretion disk,

$$V_{\max} = \sin i \left(\frac{GM_1}{R_{\min}} \right)^{1/2},$$

indicates that the radius R_{\min} at the inner edge of the emission line region is greater than the photometric radius R_1 of the primary star by an amount ranging from 1.9 to 3.1 depending on the model. This constraint is sometimes used in combination with the Hamada-Salpeter relation to place lower limits on white dwarf masses; in the case of Z Cha it is not a very restrictive constraint.

The velocity splitting between the two emission line peaks is $2V_{\min} = 1200 \pm 50 \text{ km s}^{-1}$ for the H α line (Marsh, Horne, and Shipman 1987) and also for the Ca II infrared triplet (Fig. 6). The observed splitting increases to $\sim 1400 \text{ km s}^{-1}$ for higher members of the Balmer series, but this effect appears to be due to a superposition of broad Balmer absorption lines from the white dwarf. If we interpret the observed splitting as due to the Keplerian velocity of material at the outer edge of the disk, then the outer disk radius is given by

$$\frac{R_{\max}}{a} = \left(\frac{K_2}{V_{\min}} \right)^2 (1 + q).$$

Table 4 shows this R_{\max} to be larger than R_{bs} by amounts ranging from 1.3 to 2.2, i.e., the small observed velocity split-

ting implies that the emission-line region extends well outside the bright spot radius. Marsh, Horne, and Shipman (1987), however, observed eclipses of the emission at the two peaks, which demonstrated that this emission originates from inside $\sim 0.4a \sim 1.2R_{\text{bs}}$. To reconcile these observations would require that velocities in the outer disk appear to be sub-Keplerian by $\sim 25\%$.

According to current ideas (e.g., Paczyński and Sienkiewicz 1983; Rappaport and Joss 1984), short-period binary systems such as Z Cha evolve through a minimum binary period near 80 minutes as the secondary star becomes more and more degenerate and as the timescale of mass loss eventually becomes smaller than the secondary star's thermal timescale, which reflects its ability to adjust its structure to its decreasing mass. Our measurement of M_2 places Z Cha B in the P - M_2 plane close to the evolutionary tracks calculated by, e.g., Paczyński and Sienkiewicz (1981). (Note that although the observed period of Z Cha has been increasing for the last 15 years [Cook and Warner 1981; Wood *et al.* 1986], the prediction of the gravitational radiation theory is that the period should decrease on an evolutionary time scale.) It thus appears that Z Cha B is just beginning to depart from thermal equilibrium as a result of mass transfer. The observed spectral type, near M5.5 on the Boeshaar scale, is close to that expected for its mass (e.g., Popper 1980 lists L726-8 = Gliese 65ab as an equal-component binary with masses $0.11 \pm 0.02 M_\odot$; the Boeshaar 1976 spectral type is dM6e).

The distance of Z Cha according to Bailey *et al.* (1981) is 125 ± 20 pc. This is based on infrared observations of Z Cha B and a calibration of the infrared K surface brightness of late-type stars as a function of $V-K$ color. The distance is proportional to the adopted radius of Z Cha B, which scales as $M_2^{1/3}$ for a fixed mass ratio. Bailey *et al.* used $M_2 = 0.17 M_\odot$; using our smaller mass (model K) requires the distance to be revised downward slightly to 113 ± 19 pc.

V. CONCLUSION

We have obtained time-resolved spectroscopy of the secondary star in the short-period dwarf nova Z Cha, using the CTIO 4 m telescope and a CCD detector. The simultaneous observation of variable and comparison stars with the long-slit spectrograph, and the removal of telluric water vapor absorption scaling as $(\sec z)^{0.6}$ were crucial to the success of the experiment.

Based on the ratio of TiO band strengths, the spectral type of Z Cha B is dM5.5 on the Boeshaar scale. If the band strengths are normal, Z Cha B contributes about 15% of the total light of the system at $\lambda 7500$, averaged over the out-of-eclipse orbit.

Phase variations of the TiO and Na I absorption features indicate that they are very weak on the side of the secondary star facing the primary. This uneven distribution is not explained by a simple treatment of irradiation effects, in which the spectrum of any surface element is taken to be identical to that of a main sequence star.

From cross-correlation measurements of the Na I infrared doublet, we find the velocity semiamplitude of Z Cha B to be $K_2 = 430 \pm 16 \text{ km s}^{-1}$, after a small correction for the uneven distribution of Na I absorption over the surface of the star. Combining this measurement of K_2 with the mass ratio and orbital inclination measured from eclipses by Wood *et al.* (1986), we find masses of 0.84 ± 0.09 and $0.125 \pm 0.014 M_\odot$ for

the primary and secondary stars respectively. Details of this and several other models of Z Cha are collected in Table 4.

The abundant observational constraints on Z Cha reveal that masses and other quantities of interest are quite sensitive to which subsets of the data are used and to the assumptions that are made. The spectroscopic masses are 3σ higher than masses derived from eclipse observations. If the spectroscopic masses are correct, then the primary star seen in the eclipse data appears to be $50\% \pm 15\%$ larger than a Hamada-Salpeter white dwarf. However, the velocity splitting of double-peaked emission lines indicates lower masses unless velocities in the outer accretion disk are sub-Keplerian by $\sim 25\%$. The orbital motion of the white dwarf is not reliably traced by the emission lines. Such systematic effects may bias the derived orbital parameters of many cataclysmic binaries, for which less complete observational data are generally available.

Mass transfer driven by gravitational radiation may be just beginning to drive Z Cha B away from thermal equilibrium, as it lies close to the computed evolutionary tracks in the period-mass diagram of Paczyński and Sienkiewicz (1981).

We thank the Director of CTIO for the allotment of observing time in two seasons, and the support staff of CTIO for valuable assistance in all phases of the observations. Data analysis was carried out using computers of the United Kingdom SERC STARLINK network and the STScI. R. A. W. thanks D. Lynden-Bell for the hospitality of the Institute of Astronomy, Cambridge, England, during the course of this work. G. Berriman, R. Green, J. Liebert, and J. Wood made valuable comments on a draft version of this paper. This work was supported in part by NSF grants AST 82-18624 and AST 85-14778 to the University of Arizona.

REFERENCES

- Bailey, J. 1979, *M.N.R.A.S.*, **187**, 645.
 Bailey, J., Sherrington, M. R., Giles, A. B., and Jameson, R. F. 1981, *M.N.R.A.S.*, **196**, 121.
 Barnes, T. G., and Evans, D. S. 1976, *M.N.R.A.S.*, **174**, 489.
 Bath, G. T., Evans, W. D., Papaloizou, J., and Pringle, J. E. 1974, *M.N.R.A.S.*, **169**, 447.
 Boeshaar, P. 1976, Ph.D. thesis, Ohio State University.
 Bortle, J. E. 1985a, *AAVSO Circ.* 173.
 ———. 1985b, *AAVSO Circ.* 174.
 Cook, M. C., and Warner, B. 1981, *M.N.R.A.S.*, **196**, 55P.
 ———. 1984, *M.N.R.A.S.*, **207**, 705.
 Córdoba, F. A., and Mason, K. O. 1983, in *Accretion-driven Stellar X-ray Sources* ed. W. H. G. Lewin and E. P. J. van den Heuvel (Cambridge: Cambridge University Press), p. 147.
 Curcio, J. A., Drummeter, L. F., and Knestrick, G. L. 1964, *Appl. Optics*, **3**, 1401.
 Eggleton, P. P. 1983, *M.N.R.A.S.*, **268**, 368.
 Gies, D. R., and Bolton, C. T. 1986, *Ap. J.*, **304**, 371.
 Gliese, W. 1969, *Veröff. Astron. Rechen-Inst. Heidelberg*, No. 22.
 Griffin, R. F. 1971, *M.N.R.A.S.*, **155**, 1.
 Hamada, T., and Salpeter, E. E. 1961, *Ap. J.*, **134**, 683.
 Horne, K. 1986, *Pub. A.S.P.*, **98**, 609.
 Horne, K., and Cook, M. C. 1985, *M.N.R.A.S.*, **214**, 307.
 Hessman, F. V., Robinson, E. L., Nather, R. E., and Zhang, E.-H. 1984, *Ap. J.*, **286**, 747.
 Koester, D., and Schoenberger, D. 1986, *Astr. Ap.*, **154**, 125.
 Lacy, C. H. 1977, *Ap. J. Suppl.*, **34**, 479.
 Marsh, T. R., Horne, K., and Shipman, H. L. 1987, *M.N.R.A.S.*, **225**, 551.
 Oke, J. B., and Gunn, J. E. 1983, *Ap. J.*, **266**, 713.
 Paczyński, B., and Sienkiewicz, R. 1981, *Ap. J. (Letters)*, **248**, L27.
 ———. 1983, *Ap. J.*, **268**, 825.
 Patterson, J. 1984, *Ap. J. Suppl.*, **54**, 443.
 Popper, D. M. 1980, *Ann. Rev. Astr. Ap.*, **18**, 115.
 Rappaport, S., and Joss, P. C. 1984, *Ap. J.*, **283**, 232.
 Rayne, M. W., and Whelan, J. A. J. 1981, *M.N.R.A.S.*, **196**, 73.
 Ritter, H. 1980, *Astr. Ap.*, **86**, 204.
 Robinson, E. L. 1976, *Ann. Rev. Astr. Ap.*, **14**, 119.
 Schneider, D. P., and Young, P. 1980, *Ap. J.*, **238**, 946.
 Shafter, A. W. 1983, *Ap. J.*, **267**, 222.
 Skilling, J., and Bryan, R. K. 1984, *M.N.R.A.S.*, **211**, 111.
 Stauffer, J. R., and Hartmann, L. W. 1986, *Ap. J. Suppl.*, **61**, 531.
 Stover, R. 1981, *Ap. J.*, **249**, 673.
 Vogt, N. 1982, *Ap. J.*, **252**, 653.
 Wade, R. A. 1981, *Ap. J.*, **246**, 215.
 ———. 1985, in *Interacting Binaries*, ed. P. P. Eggleton and J. E. Pringle (Dordrecht: Reidel), p. 289.
 ———. 1987, *Ap. Space Sci.*, **131**, 507.
 Warner, B. 1974, *M.N.R.A.S.*, **168**, 235.
 Watts, D. J., Bailey, J., Hill, P. W., Greenhill, J. G., McCowage, C., and Carty, T. 1986, *Astr. Ap.*, **154**, 197.
 Wood, J. 1986, Ph.D. thesis, University of Cambridge.
 Wood, J., Horne, K., Berriman, G., Wade, R. A., O'Donoghue, D., and Warner, B. 1986, *M.N.R.A.S.*, **219**, 629.
 Young, P., and Schneider, D. P. 1979, *Ap. J.*, **230**, 502.
 ———. 1981, *Ap. J.*, **247**, 960.

KEITH HORNE: Space Telescope Science Institute, 3700 San Martin Drive, Baltimore, MD 21218

RICHARD A. WADE: Steward Observatory, University of Arizona, Tucson, AZ 85721